Design considerations for a Beam Loss Monitor at the Photo Injector Test Facility at DESY in Zeuthen (PITZ)

Diplomarbeit

Humboldt Universität zu Berlin
Mathematisch-Naturwissenschaftliche Fakultät I
Institut für Physik

eingereicht von

Peter Spanknebel
geb. am 16.06.1979 in Berlin

1. Gutachter: Prof. Dr. Hermann Kolanoski
2. Gutachter: Prof. Dr. Thomas Lohse
Berlin, September 2006

Zusammenfassung

Der Photoinjektor Teststand am DESY [13] in Zeuthen (PITZ, [39]) ist ein kleiner Linearbeschleuniger der die Produktion von Elektronenpaketen in Bezug auf die transversale Emittanz und andere Strahlparameter optimiert. Der Betrieb des Teststandes mit Elektronenpaketen hoher Ladungsdichte und extrem kleiner transversaler Ausdehnung kann für den Linearbeschleuniger selbst gefährlich sein, wenn der Strahl andere Elemente des Linearbeschleunigers trifft als den Strahlabsorber am Ende der Strahlführung. Um eine Beschädigung des Teststandes zu vermeiden, wird ein System zur Strahlverlustkontrolle (Beam Loss Monitor) benötigt. Dieser soll problematische Strahlverluste erkennen und, wenn nötig, die Unterbrechung des Strahls auslösen.
Ein kurzer Überblick über bestehende Systeme zur Strahlverlustkontrolle wird gegeben. Die Anforderungen eines solchen Systems zur Strahlverlustkontrolle am PITZ werden abgeschätzt. Dabei richtet sich das Augenmerk auf den lokal begrenzten, plötzlichen Temperaturanstieg innerhalb von 800 μs in der Strahlröhre.
Ein auf szintillierenden Fasern basierendes System zur Strahlverlustkontrolle wurde entworfen und am PITZ getestet. Die beobachteten Signale sind deutlich vom Hintergrund zu unterscheiden. Die Möglichkeit der Positionsbestimmung des Strahlverlustes wurde ebenfalls betrachtet. Auch hier konnte gezeigt werden, daßsich ein auf szintillierenden Fasern basierendes System zur Strahlverlustkontrolle für den Einsatz am PITZ eignet.

Contents

1 Introduction

A Free Electron Laser (FEL) is a source of high intense, coherent, short bunched light pulses. For the lasing of a FEL, electron bunches of high charge have to pass through an arrangement of alternating magnetic fields realized in so called undulators. These electron bunches need to have extremely low transverse emittance (see Sec. 2). The Photo Injector Test Facility at DESY [13] in Zeuthen (PITZ) [39] is a small linear accelerator (linac) optimizing the production of electron beams with respect to the transverse emittance and other parameters. Operation with electron bunches of high charge at extremely small transverse beam sizes can be dangerous for the linac itself, if the beam is dumped to any other component than the absorber. To avoid damage of the facility and it's components, a Beam Loss Monitor (BLM) is needed to detect and to avoid intolerable beam losses and cause the interruption of the beam if needed.
In this work a survey on existing BLM systems with respect to the needs at PITZ has to be given. The basic needs and the requirements on a BLM system for PITZ have to be defined. In this context, the local temperature rise of the beam tube due to beam losses at different operation parameters of PITZ, has to be estimated. The BLM should allow to determine the position of the beam loss.
Concentrating on beam losses within 800 μs, the intolerable temperature rise in the beam tube is estimated. Based on this, the requirements on a BLM system for PITZ are deduced. A system using scintillating fibers was designed and tested in laboratory, at DESY3 in Hamburg and at PITZ. The possibility to estimate the position of the beam loss with the scintillating fibers was tested as well. Monte Carlo calculations were applied to supplement and understand the measurements.

2 Photo Injector Test Facility at DESY in Zeuthen (PITZ)

Electron bunches are short packages of high electron density. PITZ aims for 0.9 π mm mrad normalized transverse emittance at 1 nC charge per bunch. Up to 7200 bunches in a train of up to 800 μs length will be repeated with a rate of up to 10 Hz. The electrons are aimed to have a maximum momentum of 40 MeV/c.

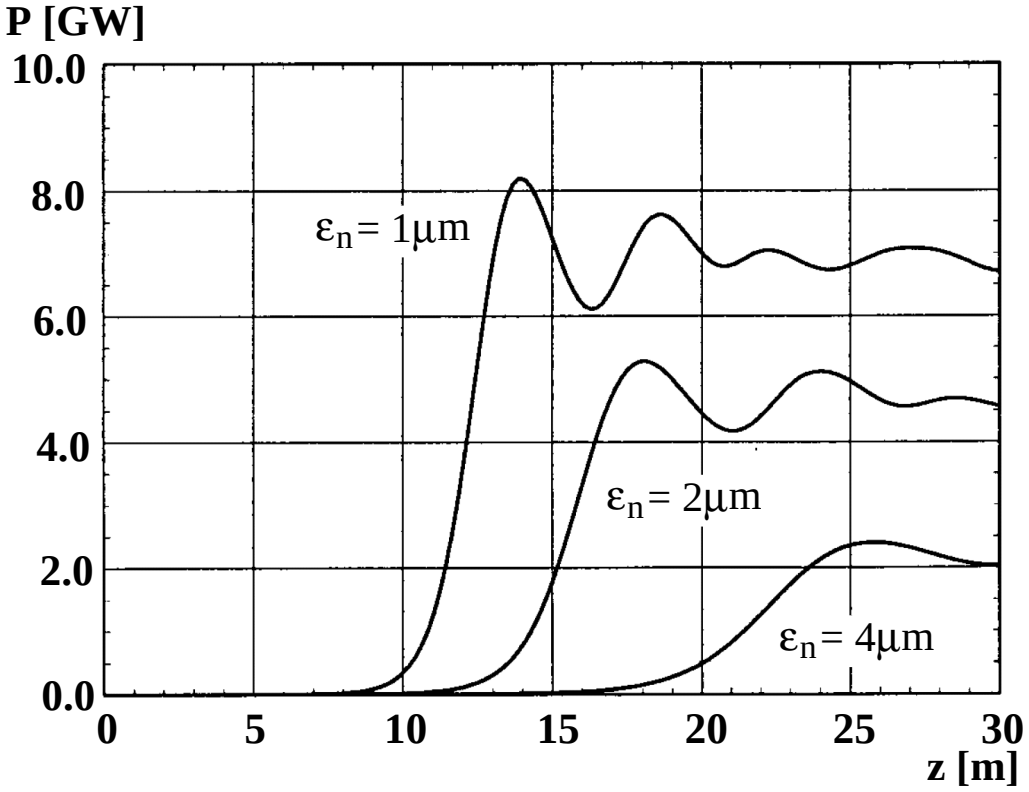

Figure 1: Dependence of the output radiation power P of a FEL on the normalized beam emittance ϵ_n for the example of the TTF FEL at $\lambda = 6.4nm$. The energy width $\frac{\Delta E_e}{E_e}$ of the electron beam is 0.1 %. The path length of the electron in the undulator is z. The plot was taken from [25] and slightly restaurated.

As mentioned in Sec. 1, Free Electron Lasers (FELs) need amongst other things electron bunches of extremely low transverse emittance. The transverse emittance is a measure for the area occupied by the electron beam in the phase space. For the x direction the emittance is defined as

$$\epsilon_x = \sqrt{\langle x^2 \rangle \cdot \langle x'^2 \rangle - \langle x \cdot x' \rangle} \quad (1)$$

$$\text{with } x' = \frac{dx}{dz} \quad (2)$$

and for the y direction respectively. Following Liouvilles theorem, the emittance is often normalised with $\frac{1}{\beta\gamma}$ where

$$\beta = \frac{v}{c} \quad (3)$$

$$\gamma = \frac{1}{\sqrt{1-\beta^2}} \quad . \tag{4}$$

Extremely small transverse beam sizes are connected to low transverse emittance via (2). As shown in Fig. 1, the saturation level of the output power of a FEL is falling with rising emittance, while the needed travelling length in undulators increases. Longer undulators would be more expensive themselves, but extending the tunnel would blow up costs for a FEL. The variation of the undulator length would not increase the output power saturation level anyway. In linear accelerators, the emittance produced at the source determines the emittance available for the FEL.

The PITZ linac consists of a 1.5 cell normal conducting copper gun cavity (GUN), a normal conducting 9 cell booster cavity (BOOSTER), several diagnostic elements and an absorber at the end of the beam line. A scheme of PITZ is shown in Fig. 2 [37]. As shown there, the beam line is around 13 m long. It is planned to extend the beam line up to 18 m [37].

The electron bunches are produced via the photoelectric effect induced by an ultravio-

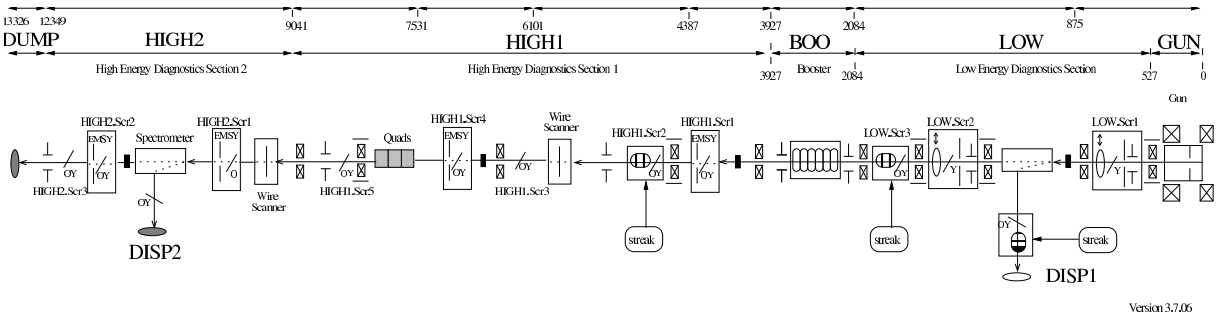

Figure 2: Schema of PITZ (status after second upgrade).

let ($\lambda = 263nm$) laser hitting a Cs_2Te photocathode. The photocathode is located at the beginning of the GUN. The GUN and the attached beam line are kept at Ultra High Vacuum (UHV) of lower than 10^{-9} mbar during operation. Especially the cathode has to be protected from vacuum higher than 10^{-8} mbar. The laser pulses are coupled into the vacuum system through a vacuum window and are directed to the photocathode with a mirror. Radio Frequency (RF) with a peak power of 4.3 MW at the cathode and a frequency of 1.3 GHz is coupled into the GUN via a special coaxial coupling device to provide an accelerating field for the electron bunches emitted from the cathode. The electron bunches are accelerated immediately after emission, which reduces the effect of expansion due to space charge. A magnetic field applied in the GUN compensates this effect in addition. After few diagnostic devices following the GUN, the electron bunches enter the BOOSTER. While the electrons have roughly 5 MeV after the GUN, the BOOSTER provides additional acceleration up to 12 MeV. Behind the BOOSTER further diagnostic stations are mounted. For some of the elements of the PITZ beam line the longitudinal positions [37] (z-positions) are listed in Table 1.

The beam tube has typically an outer diameter D_{outer} of 42 mm and an inner diameter D_{inner} of 38 mm and is made of steel (Remanit 4306 [42]). Diagnostic stations mounted along the beam line have different transverse dimensions in the order of decimeters. Support frames and flanges between diagnostic stations and the beam tube cause unsteady

device	position [cm]
cathode surface	0.0
GUN	18.9
BOOSTER	355.3
HIGH1.ICT1	418.7
EMSY1 slit mask	428.7
Wire of Wirescanner	570.4
HIGH1.ICT2	653.1
EMSY2 slit mask	663.1

Table 1: Longitudinal positions of some devices of PITZ (status after second upgrade). For extended devices the end position is given. EMSY1 and EMSY2 are named HIGH1.Scr1 and HIGH1.Scr4 in Fig. 2.

transverse dimensions too. Fig. 3 is a photograph of the beam line and may give a better impression of transverse extensions of the beam line than words can do.

Some of the diagnostic devices were used in the Beam Loss Monitor (BLM) measurements. These are described with respect to the need for these measurements:

- **Integrating Current Transformators (ICTs)**
  ICTs [6] are devices for beam charge measurement. They act as current transformators with their housing as primary coil and a solenoid inside the housing as secondary coils. An ICT gives a signal proportional to the overall charge of particles passing through it. This also includes secondary particles produced by beam losses and passing through the ICT. So, if secondary or lost particles occur near to the ICTs these might be included in the measured charge [8]. A photograph of an ICT is given in Fig. 18.

- **Wirescanners**
  A tungsten wire of 30 μm diameter is fixed between the legs of a fork. It can be inserted to the beam line by a motor driven device. The shower produced by the interaction of the electrons with the wire is detected outside the beam tube by a scintillator plate few decimeters behind the Wirescanner. The light output of the scintillator is proportional to the beam profile. The Wirescanners are used to estimate the transverse position of the beam and it's profile.

- **Emittance Measurement SYstem (EMSY)**
  Several EMSY stations are mounted along the beam line. The EMSYs measure the emittance of the electron bunches inserting slit masks of 1 mm tungsten into the beam line via a motor driven device. Most of the electrons are stopped by the slit mask. Electrons passing the slit are visualized with a fluorescent screen. Their distribution is used to estimate the emittance of the beam.

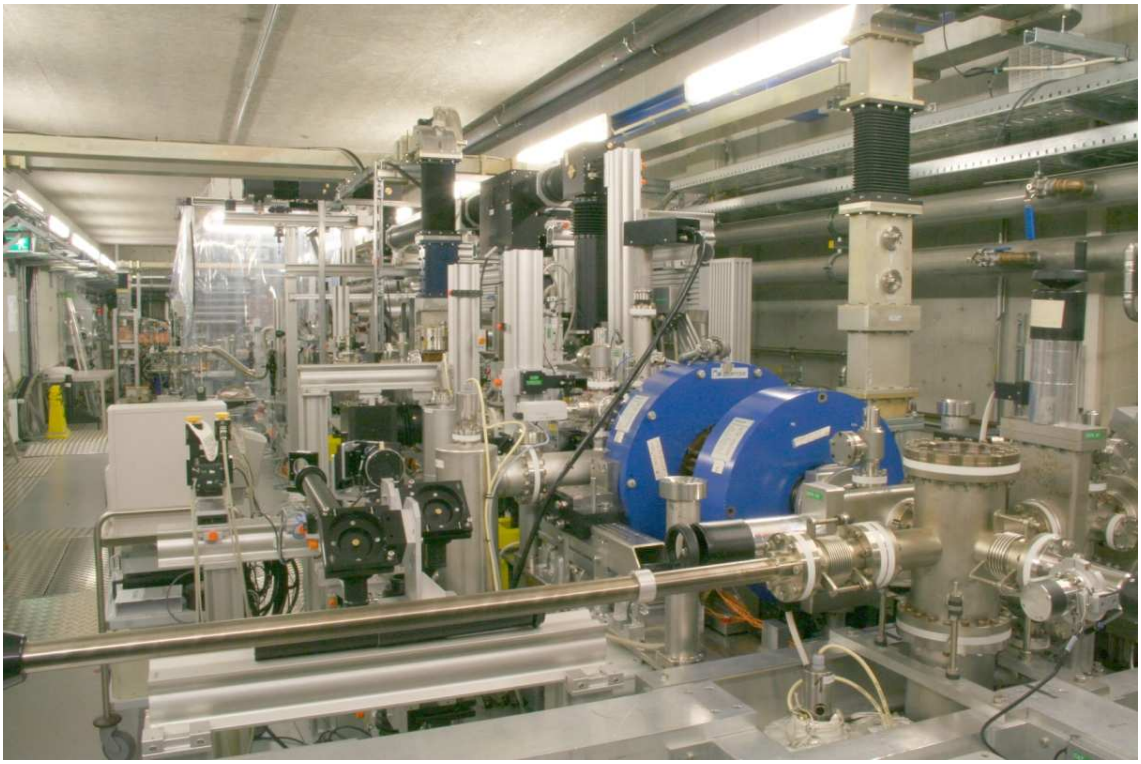

Figure 3: Photograph of the PITZ beam line. The blue rings are magnets at the GUN. From above, the RF waveguides power the GUN and the BOOSTER.

The time structure of the electron bunches equals the time structure of the laser micropulses. The same is true for bunch trains and macropulses. A macropulse of 800 μs length as shown in Fig. 4, consists of several micropulses. Each micropulse is approximately 25 ps long. The maximum number N_m of micropulses in a macropulse and the time Δt_1 between the micropulses depend on the frequency ν_{laser} of the laser. The laser can be operated at 1 MHz. The design goal of 9 MHz for the laser has to be taken into account, although not possible in the current upgrade status of the laser. The repetition of the macropulses is adapted to the repetition rate of the RF System. A set of operation parameters is summarized and assigned to the resulting mean current I in Table 2.
Besides these operation modes, any wanted number of bunches per train $N_{b/train}$ with

$$N_{b/train} \leq N_m \tag{5}$$

can be realized. Typically, a bunch train made of up to hundred bunches of 1 nC charge is used for the measurements at PITZ. 7200 bunches will be possible in the future and have to be taken into account for the design of the BLM.

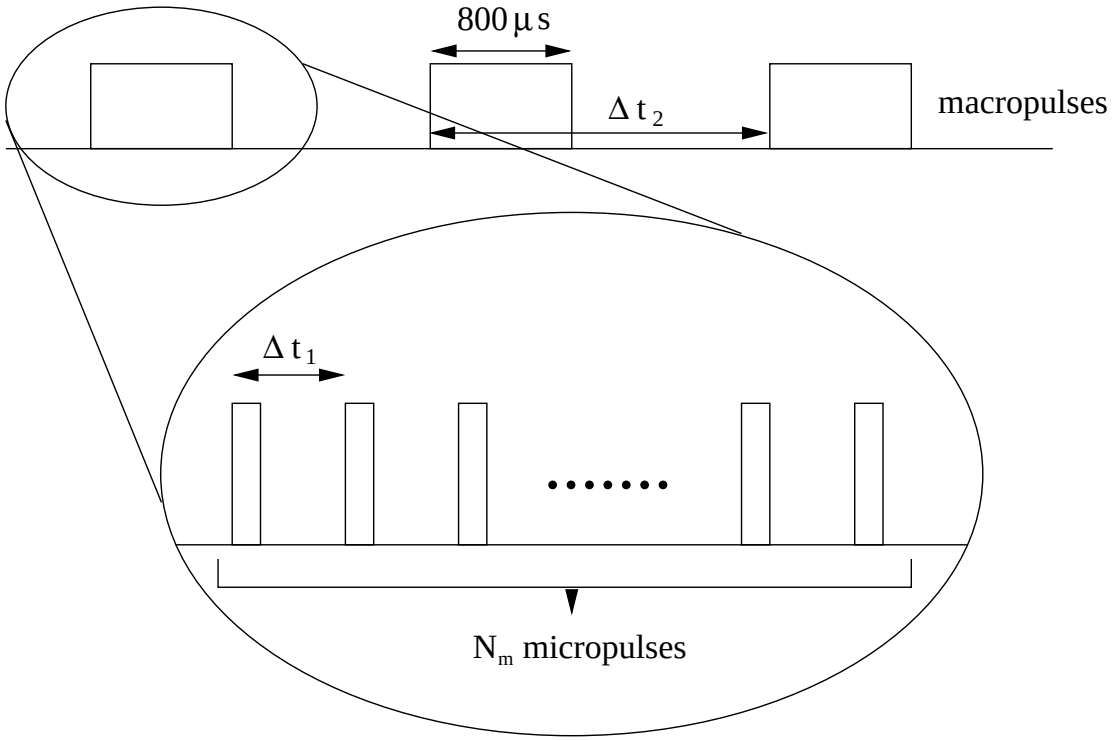

Figure 4: The time structure of the laser at PITZ. The values for Δt_1 and Δt_2 for given ν_{laser} and $\nu_{repetition}$ are listed in Table 2.

ν_{laser} [MHz]	N_m	Δt_1 [μs]	$\nu_{repetition}$ [Hz]	Δt_2[s]	I [μA]
1.0	800	1.0	1.0	1.0	0.8
1.0	800	1.0	2.0	0.5	1.6
1.0	800	1.0	10.0	0.1	8.0
9.0	7200	0.11	1.0	1.0	7.2
9.0	7200	0.11	2.0	0.5	14.4
9.0	7200	0.11	10.0	0.1	72.0

Table 2: Mean current I in the PITZ linac. A charge of 1 nC for each micropulse was assumed. Δt_1 and Δt_2 correspond to Fig. 4

3 Beam losses and their impact at PITZ

An accidental loss of a beam can not be excluded at such complex machines like PITZ. The losses can be grouped into fast and slow losses [45]. Slow losses occur mainly in circular machines, where a certain fraction of the beam is lost every revolution. For the PITZ linac, slow losses are a minor problem, because only few electrons are lost spread over a relatively large area. Fast losses include the complete loss of the beam into some of the machine components concentrated on a small area.
The worst case, that has to be considered for PITZ occurs with the following set of parameters.

- **High charge**
  Electron bunches of 1 nC charge are a main item of the PITZ design values. The current status of laser and cathode allows charges up to 1.3 nC per bunch. Improved cathodes or upgrades of the laser may result in charges higher than 1.3 nC per bunch in the future.

- **Small transverse beam size**
  In extreme cases, beam sizes of 20 μm can not be excluded in the final state of PITZ.

- **High electron energy**
  The design goal for PITZ is an energy of 40 MeV per electron.

- **High rate of bunches**
  In the final state, the laser will be able to produce 7200 pulses per train, i.e. 7200 electron bunches within 800 μs will be transported through the beam tube.

For the elements of the PITZ beam line, the highest risk is the local heating at the position where a beam of small size goes into the material. The time domain for instantaneous temperature rise ΔT_{inst} can be defined as $\leq 800\mu s$, which is within one bunch train. Longterm heating of the material can harm the machine as well as instantaneous temperature rise. Here, several bunch trains have to be considered. Heat transfer from the central impact volume beneath the *hot spot* to the surrounding material acts as cooling effect for the hottest region. Effects contributing to the heat transfer are

- **heat conduction,**
  Based on Fourier's law, the conductive transfer of heat dQ per time unit dt is proportional to the contact surface $A_{contact}$ and the temperature gradient $\frac{dT}{dx}$ with the thermal conductivity η [44]

$$\frac{dQ}{dt} = \eta \cdot A_{contact} \cdot \frac{dT}{dx} \quad . \tag{6}$$

- **convection and**
  Particles whose kinetic energy exceed the work function of the material, can leave either into the vacuum or the air. They can carry some energy with them, which results in a net cooling for the heated volume [11].

- **radiative cooling.**
  Radiation emitted by the heated volume introduces an additional cooling. This effect will be rather small compared to the previous ones due to small contact area to air and vacuum. On the other hand, the emitted power is proportional to T^4.

These cooling effects have to be considered for longterm heating starting from approximately $800\mu s$.
The upper temperature limit for the beam tube is it's melting point $T_{melt} \approx 1700K$. Degradation of the vacuum might be caused by temperature rise below T_{melt}. This has to be prevented, because vacuum above 10^{-8} mbar destroys the properties of the photo cathode. For the case of an instantaneous temperature rise there is no information on outgassing or melting available. The producer of the steel announces [42], that a continuous operation at 350 K, which equals

$$\frac{T_{melt} - 300K}{4} = 350K \tag{7}$$

is possible. Hence, an instantaneous temperature rise of

$$\Delta T_{inst} = 350K \tag{8}$$

is considered as upper limit.

The lowest temperature rise that can harm the beam tube is deduced from Hook's law. In the range of small expansion $\Delta L \ll L$ the tension τ is proportional to the strain $\epsilon = \frac{\Delta L}{L}$ with the coefficient of elasticity E

$$\tau = E \cdot \epsilon = E \cdot \frac{\Delta L}{L} \quad . \tag{9}$$

In combination with the coefficient of thermal expansion α, which is defined as

$$\alpha = \frac{1}{L} \cdot \frac{\Delta L}{\Delta T} \tag{10}$$

in the linear case, the expression

$$\Delta T = \frac{\tau}{E \cdot \alpha} \tag{11}$$

can be derived. Using the technical elastic limit $R_{0.2}$ as maximum allowed tension, results in

$$\Delta T_{elastic} = \frac{R_{0.2}}{E \cdot \alpha} \quad . \tag{12}$$

The index of the elastic limit denotes, that the relative expansion caused by this tension is limited to 0.2 %. At this level the deformation is still reversible. For the steel [42] of the PITZ beam line we find $\Delta T_{elastic} \approx 56K$. In addition, $\Delta T_{elastic}$ should be cut down to 50 K per bunch for PITZ. Below $\Delta T_{elastic}$ the steel parts of PITZ will not be damaged, because deformations due to the temperature rise are still elastic. If the temperature rise is above $\Delta T_{elastic}$, it has to be assured that the beam will not hit this position frequently. Otherwise the steel will loose it's properties like vacuum tightness and robustness at this position after some time.
Hence, the BLM must prevent instantaneous temperature rise ΔT_{inst} higher than 350 K to assure that the steel does not melt. Below 50 K the mechanical stress due to local heating is reversible and the BLM is not needed.
To simplify the further calculations the beam tube is assumed to be made of iron. The difference in nuclear properties is negligible.
Neglecting any cooling effects with respect to the short time range of the heating process,

the instantaneous temperature rise due to energy loss in iron of 2 mm depth (which equals the typical thickness of the beam tube's wall) can be estimated by

$$\Delta T_{inst} = \frac{n_{elec} \cdot dx}{V \cdot c} \cdot \frac{dE}{\rho dx} \quad . \tag{13}$$

Here, dx the thickness of the material, V the volume beneath the hot spot and c = 0.5 $\frac{J}{gK}$ the specific heat capacity of iron. The number of electrons n_{elec} in (13) considers the number of electrons entering the considered volume. Roughly 39% of the electrons of a two-dimensional Gaussian distributed beam will be included in the range of 2σ around the mean. Considering a cylindric volume of 2σ cross section,

$$n_{elec} \approx N_{b/train} \cdot \frac{Q \cdot 0.39}{e} \tag{14}$$

is the number of electrons per bunch train with bunches of charge Q contributing to ΔT_{inst} of (13). Fig. 5 shows the temperature rise ΔT_{inst} in a cylindric iron volume of 2σ diameter for different numbers of bunches as function of the beam size σ.

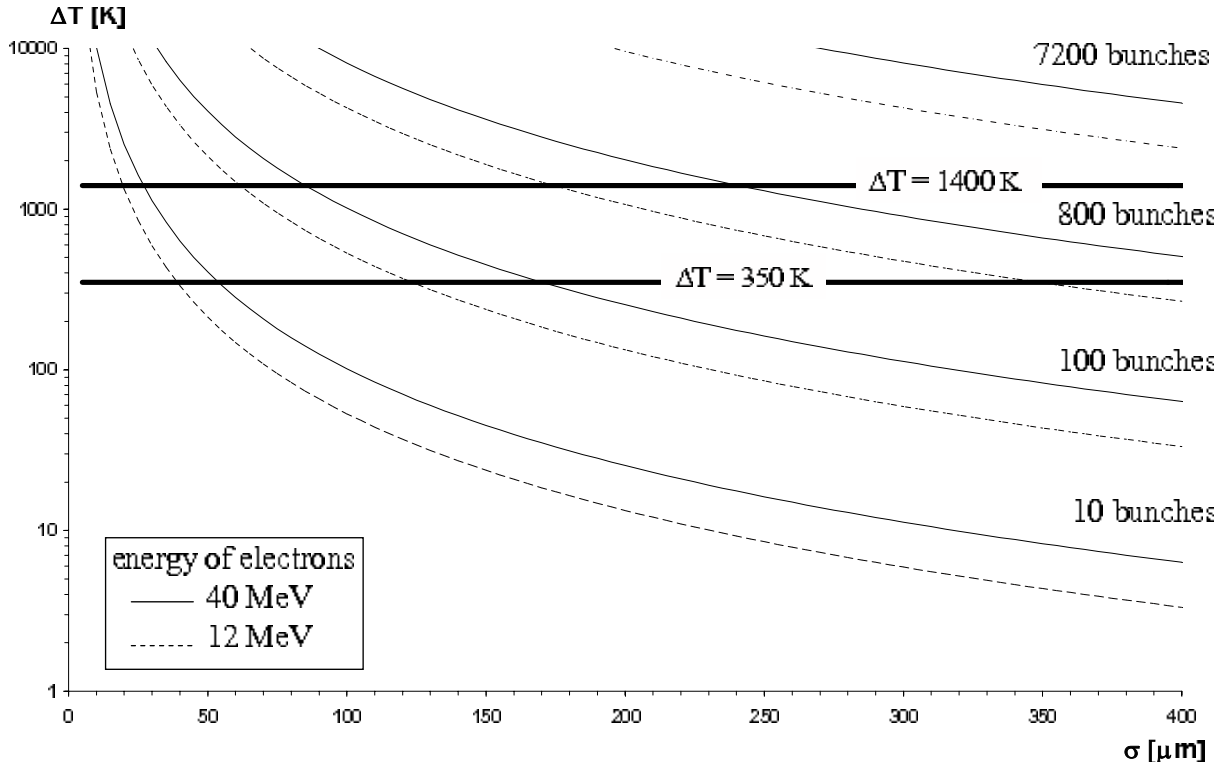

Figure 5: Instantaneous temperature rise ΔT_{inst} plotted against the beam size σ for different amounts of 1 nC bunches. While an energy of 40 MeV for the electrons is the design value for PITZ, in the present stage max. 12 MeV can be reached. Note, that the number of bunches is included in n_{elec} of (13). Starting from 50 K operation might harm the machine. $\Delta T_{inst} > 350K$ has to be prevented.

The interaction of the beam with iron was also simulated with GEANT (see Appendix C.1) and FLUKA (see Appendix C.2) yielding to lower ΔT_{inst} than with (13). These calculations are based on Gaussian beams directed to cylindric volumes of 200 μm length and σ radius. The finite binning might cause the lower values of ΔT_{inst}.

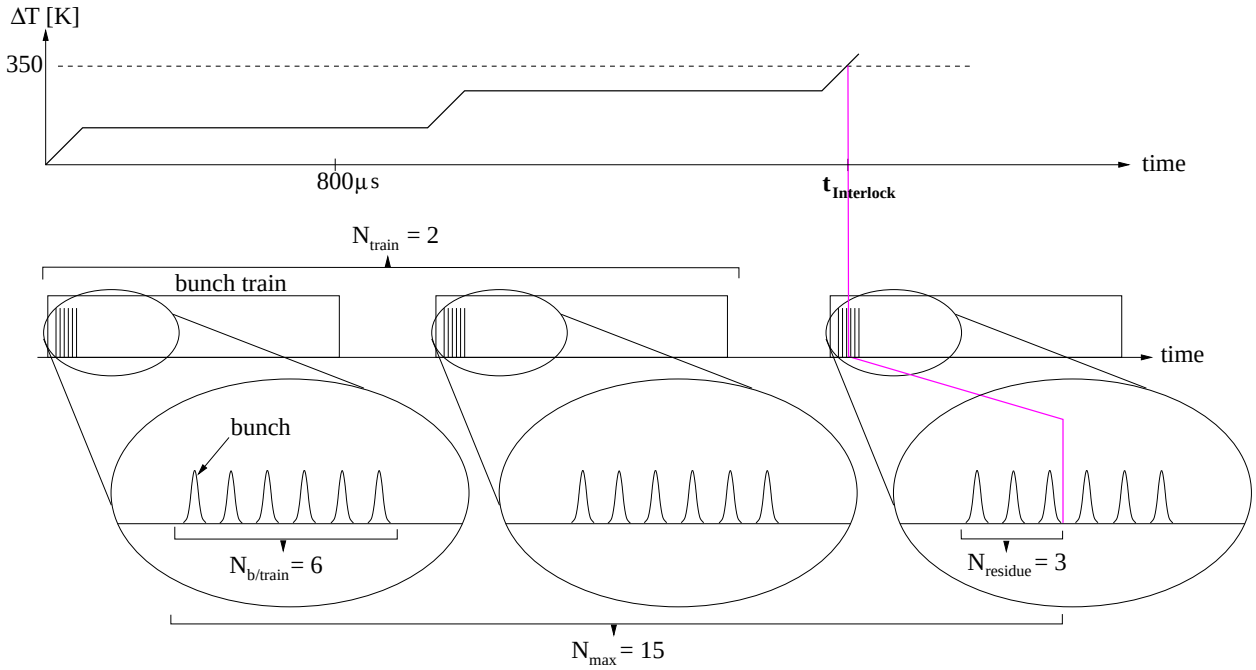

Figure 6: Illustration of the variables N_{max}, N_{train}, $N_{b/train}$ and $N_{residue}$ needed for (18). Here an example of $N_{b/train} = 6$ and $N_{max} = 15$ is choosen. Note, that the time axis is not in scale. The time between two subsequent bunch trains will be much longer (depending on $\nu_{repetition}$) than illustrated here. The temperature curve is just a plain illustration and does not show the real development of ΔT.

Depending on the particular PITZ operation parameters, different loss limitations have to be defined. The time until the subsequent electron bunches hitting the beam tube cause an temperature rise ΔT_{inst} just below 350 K is called $t_{Interlock}$.
The following formula (18) can be used to calculate $t_{Interlock}$ for any number $N_{b/train}$ of bunches per train (see Fig. 6 for a graphical illustration). Note, that $t_{Interlock}$ is the time, in which the intolerable beam loss occurs. A BLM needs to be faster than this and stop operation within $t_{Interlock}$.

$$N_{max} = \left[\frac{350K \cdot e \cdot \pi \cdot \sigma^2 \cdot c}{Q \cdot 0.68 \cdot \frac{dE}{\rho dx}} \right] \tag{15}$$

denotes the maximum number of allowed bunches[1] based on (13) and (8). Q is the charge per bunch and c the specific heat capacity. The number of complete bunch trains that are allowed

$$N_{train} = \left[\frac{N_{max}}{N_{b/train}} \right] \tag{16}$$

[1] the integer part [47] of a number is denoted with $[number]$

E_{e^-} [MeV]	σ [cm]	$N_{b/train}$	ν_{Laser} [MHz]	N_{max}	N_{train}	$N_{residue}$	$t_{Interlock}$
40	0.004	7200	9.0	5	0	5	0.56 μs
40	0.02	7200	9.0	137	0	137	15.2 μs
40	0.02	50	9.0	137	2	37	200 ms
40	0.02	10	1.0	137	13	7	1.3 ms
40	0.0015	1	1.0	0	0	0	–
12	0.002	7200	9.0	2	0	2	0.22 μs
12	0.02	800	1.0	262	0	262	262 μs
12	0.02	150	1.0	262	1	112	100 ms
12	0.2	100	1.0	26263	262	63	26 s
12	0.02	10	1.0	262	26	2	2.6 s
12	0.2	10	1.0	26263	2626	3	262 s
5	0.004	100	1.0	13	0	13	13 μs
5	0.02	10	1.0	344	34	4	3.4 s
5	0.2	10	1.0	34424	3442	4	344 s

Table 3: The maximum number of full bunches (N_{max}) allowed to stay below the $\Delta Tinst = 350K$ and the corresponding time interval $t_{Interlock}$ in which these bunches occur, are listed here for different operation modes. A charge of 1 nC per bunch was assumed. The values are based on (18). $t_{Interlock}$ is given in reasonable accuracy w.r.t. the time domain.

is given by the integer part [47] of the ratio of N_{max} and $N_{b/train}$.
After N_{train} bunch trains, the number of residual allowed bunches is

$$N_{residue} = N_{max} - \left(N_{train} \cdot N_{b/train}\right) \quad . \tag{17}$$

With $\nu_{repetition}$ as the repetition rate of the bunch trains the estimation of $t_{Interlock}$ is

$$t_{Interlock} = \frac{N_{train}}{\nu_{repetition}} + \frac{N_{residue}}{\nu_{laser}} \quad . \tag{18}$$

For example, a 40 MeV electron bunch with $\sigma = 200\mu m$ and 1nC hitting the tube wall, causes a temperature rise of $\approx 2.54K$. With 7200 bunches per train ΔT_{inst} is approximately $18 \cdot 10^3 K$ within 800 μs. Therefore the beam has to be interrupted within

$$t_{Interlock} \approx 15.2\mu s \tag{19}$$

(137 bunches) which corresponds to $\Delta T_{inst} \approx 350K$.
If only few bunches are included in one train, the time domain may justify the application of effects yielding to cooling of the heated volume. This longterm heating results in a longer $t_{Interlock}$ than given by (18).
$t_{Interlock}$ was calculated based on (18) for different operation modes of PITZ. Some sets of different parameters in Tab. 3.

An energy of 5 MeV is reached at PITZ if only the GUN is powered with RF. If beam sizes in the order of 40 μm appear, interruption is needed within 13 μs, i.e. 13 bunches at $\nu_{laser} = 1MHz$ at this energy. $t_{Interlock}$ calculated with (18) shows, that damage of the machine can be excluded for beam sizes around 200 μm, because cooling effects will lower

the temperature at the hot spot in the time domain of seconds. If cooling balances the heating, a stable temperature below 350 K will be reached after some time.
If, in addition to the GUN, the BOOSTER is operated, an energy of 12 MeV can be reached up to now. At this energy, operation is uncritical at 10 bunches per train. Starting with 150 bunches per train at beam sizes of $\sigma = 200\mu m$ the beam has to be interrupted within the second bunch train (see Tab. 3). Effects yielding to cooling of the heated volume will already be important in the time domain of milliseconds.
At the energy of 40 MeV extremely small beam sizes can be reached. Note, that if the beam hits the beam tube at $\sigma = 15\mu m$ the beam would have to be stopped within the first bunch (see Tab. 3) to stay below $\Delta T_{inst} = 350K$. This is not possible and the operators of PITZ have to take care themselves to prevent such situations (see Sec. 7).

4 Beam Loss Monitor systems

Beam Loss Monitor (BLM) systems are used to detect the particles produced in showers of partial or complete loss of accelerated particles. The monitoring of the dose rate [31] is common as well as the monitoring of single pulses [14,33].
The concept of most BLMs is to detect the electromagnetic shower (see Appendix B) produced by the loss of the beam into the wall of the vacuum chamber or other parts of the beam line. A fraction of the electrons produced in these showers can be detected by the sensitive parts of the BLM due to their energy loss. Some ways to detect this energy are described in the following sections.
Different approaches of BLMs can be grouped to discrete and continuous BLM systems. The monitoring of special, selected points or parts of a beam line can be done with discrete BLM systems. If the whole beam line has to be monitored, either many discrete BLMs or a continuous BLM is needed.

4.1 Beam Loss Position Monitors

Beam Loss Position Monitors (BLPM) offer the feature to determine the position of the beam loss. This is not necessarily included in all BLMs.
For discrete BLMs, the longitudinal and transverse position of the beam loss is given by the position of the detector. In the case of continuous detectors, advanced methods have to be applied if the BLM should inform about the longitudinal position of the beam loss. If fibers are used to detect the showers at linear accelerators, the following two methods are thinkable.

- **Time measurement**
  Either the difference of the arrival time of the pulses from both sides of the fiber might be measured or the difference of the arrival times of the direct and the reflected pulse (see Sec. 4.4.2).

- **Measurement of the amplitude**
  Here the fibers are read out from both sides and the ratio of the resulting signal amplitudes should allow the estimation of the position of the beam loss (see Sec. 4.4.3 for the principle).

Estimations on the transverse position of the beam loss can be achieved by distributing four fibers around the beam tube [33], as for example shown in Fig. 10 and illustrated in Fig. 11.

4.2 A BLM system for PITZ

PITZ needs a BLM system including longitudinal and transverse position estimation of the beam loss. The main tasks of a BLM at PITZ are

- to avoid intolerable losses,

- to inform about the location of any losses with an error of $\pm$ 50 cm,

- to detect off-axis beams before they could be lost.

The whole beam line needs to be monitored continuously to fulfill these goals. The beam loss has to be detected before the lost particles can damage the components of the machine. Referring to Tab. 3, the BLM has to be able to interrupt the operation within few bunches. Therefore the dead time, when new signals can not be interpreted due to recovering of the detector, has to be lower than 0.11 μs. Otherwise single pulses could not be detected at $\nu_{laser} = 9MHz$ (see Table 2).
Being a test facility, PITZ is under steady improvement. The elements of the beam line might be exchanged from time to time for this purpose. A BLM should therefore be easy to dismount during mechanical work on the beam line and to remount afterwards.

4.3 Implementations of discrete BLM systems

Possible detectors for discrete BLMs are based on scintillator plates, ionisation chambers, Aluminium Cathode Electron Multipliers (ACEM)[2] and PIN (Positive Intrinsic Negative) Photodiodes [45].
An example of a discrete BLM is the detector manufactured by the company BERGOZ [6]. They offer a BLM based on two PIN diodes mounted face to face. While many photons

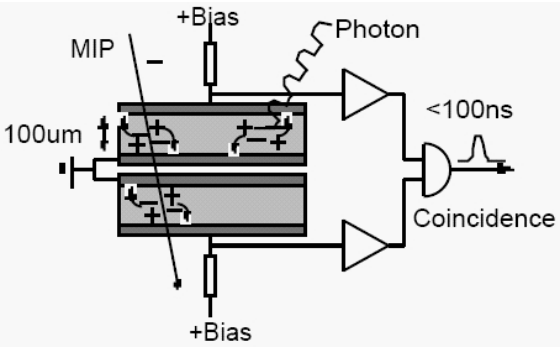

Figure 7: Principle of operation of the BERGOZ BLM. The picture was taken from the manual [7].

Figure 8: Photograph of the BERGOZ BLM mounted in iron housing together with needed electronics.

will be stopped in the first PIN diode, minimal ionising particles (MIPs) will penetrate both diodes and give signals there. The coincidence of the two signals has a reduced background from photons. If the measurements are disturbed by X-ray background, the BLM needs more shielding than the housing shown in Fig. 8 provides [6].

4.4 Implementations of continuous BLM systems

Following the concept of continuous beam loss monitoring three important technical implementations have to be mentioned. The main ideas of these three BLM systems are described in the following.

[2] applied in the CERN-PS and the PS-Booster

4.4.1 BLM system based on Long Ionisation Chambers

The Long Ionisation Chamber (LIC) is basically an air filled coaxial cable operated as ionisation chamber. In an ionisation chamber, charged particles cause the local ionisation of the chamber's gas. Ionised pairs are separated applying voltage between the anode wire and the camber wall. The type of cable suitable for this purpose is commercially avail-

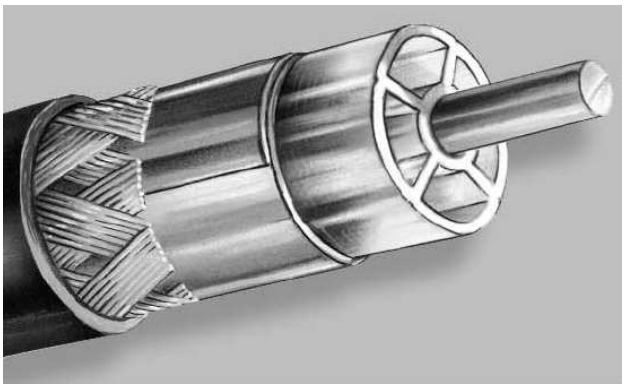

Figure 9: Picture of a cable suitable for BLM use. The picture was taken from the datasheet [1].

able [1]. The technique of these kind of BLM is approved for example at the radiation source ELBE [18] where the beam is continuous (Continuous Wave *(CW)* mode) with a mean current of 64 mA. For PITZ this kind of BLM is not promising, as PITZ has a pulsed beam with a maximum mean current of 72 μA.

4.4.2 BLM system based on the Cherenkov effect in optical fibers

Charged particles travelling through matter with a velocity higher than that of light in this matter, generate Cherenkov light. A fraction of the light generated by the passing electrons is trapped in the fiber via total reflection. This part travels in both directions through the fiber. The read out is done by a Photo Multiplier (PM) in upstream direction. Measuring the arrival times from both sides of the optical fiber is not useful, because subsequent losses in the downstream direction could overlap. Looking on the direct pulse in the upstream direction and the reflected pulse from the other end of the fiber, the position of the beam loss can be calculated [33] from the different arrival times. As the reflected light has to travel long distances in the fiber, the attenuation length λ_{att} (see Sec. 5.1.1) should be as low as possible. Systems like this are used for example at FLASH [24] or at DELTA [14] and are working well. A photograph of the fibers placed along the beam line of FLASH is given in Fig. 10. At FLASH and DELTA the systems are not used for machine protection in case of sudden beam loss but for *tuning*, i.e. localise beam losses to determine the useful beam steering knobs. At FLASH, a system for machine protection based on many discrete BLMs was installed before the Cherenkov system was available [34].
The fibers used at FLASH are commercially available, radiation hard and generate Cherenkov light for electrons with energies above 175 keV [33]. To estimate, if this system is suitable for PITZ the lowest electron energy for which signals are needed from the BLM (5 MeV) was assumed. A GEANT simulation scored the number of electrons and their

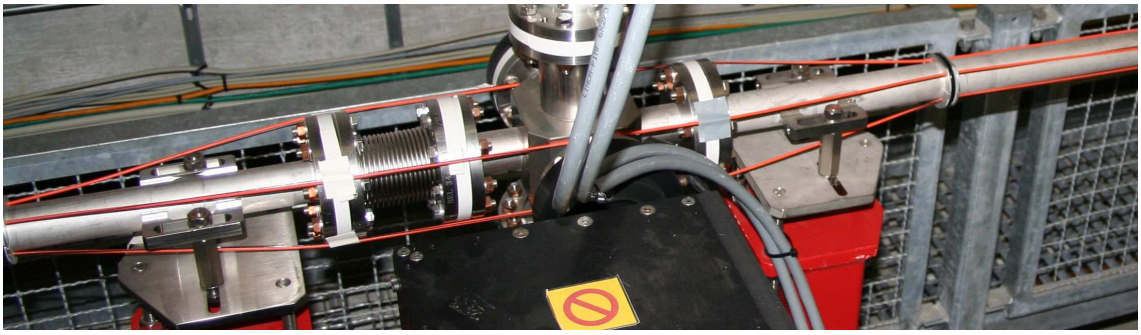

Figure 10: Photograph of the optical fiber BLPM at FLASH. The fibers are feeded in red and black plastic tubes.

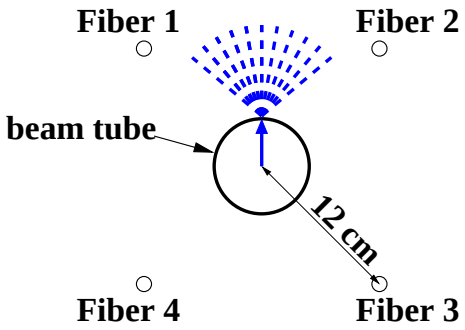

Figure 11: Sketch of the alignment of the fibers relative to the beam loss and the beam tube. The situation shown, is the worst case w.r.t. the transverse position of the beam loss.

energy when entering the fibers. The fibers are feeded along an iron tube in a PITZ geometry. The alignment around the beam tube is illustrated in Fig. 11. An electron beam of $6 \cdot 10^7$ electrons ($\approx 9.6pC$) with 5 MeV was directed to the beam tube. According to this simulation roughly 10^3 electrons above 175 keV enter Fiber 1. Extrapolating the number of electrons to $6.24 \cdot 10^9$ (equivalent to a beam charge of $\approx 1nC$), approximately 10^5 electrons that are able to generate Cherenkov light are estimated. The same is true for Fiber 2. For Fibers 3 and 4 less electrons are estimated from the simulation, because these fibers are at the opposite side of the beam loss. But for 1 nC still $5 \cdot 10^4$ electrons are predicted for these fibers. Test measurements at PITZ in coordination with FLASH were foreseen but had to be postponed.

4.4.3 BLM system based on scintillation fibers

The scintillation light generated from the deposited energy is partly transported along the scintillation fibers and connected via optical fibers to Photo Multipliers (PMs) located on both ends of the optical fibers. The mechanism of scintillation light generation is described in detail in Appendix A. Details on the setup are given in Sec. 5.
The method to determine the position of the beam loss is assuming the attenuation of an initial scintillation light amplitude A_0 along a fiber is constant. Then the fraction of A_0 which is trapped in the fiber by internal reflection can be called A_{left} and A_{right} . One can

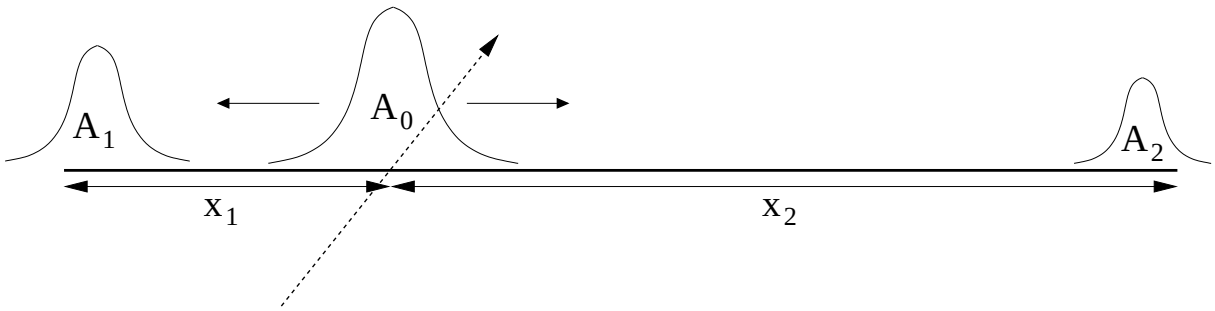

Figure 12: Particle crossing a fiber.

assume that the amount of light travelling to both sides of the fiber is equal

$$A_{trapped} \equiv A_{trap} = A_{left} = A_{right} \quad . \tag{20}$$

So the attenuated amplitude A_1 after a certain travelling distance z_1 in the fiber can be written as

$$A_1 = A_{trap} \cdot e^{-\frac{z_1}{\lambda_{att}}} \quad . \tag{21}$$

λ_{att} is the attenuation length of the fiber (see Sec. 5.1.1).
The problem of the unknown amplitudes A_{trap} can be solved if the amplitude A_2 corresponding to a different travelling length z_2 in the fiber is known in addition. The ratio of the amplitudes delivers

$$\frac{A_1}{A_2} = \frac{A_{trap} \cdot e^{-\frac{z_1}{\lambda_{att}}}}{A_{trap} \cdot e^{-\frac{z_2}{\lambda_{att}}}} = e^{-\frac{z_1 - z_2}{\lambda_{att}}} \tag{22}$$

$$ln\left(\frac{A_1}{A_2}\right) = -\frac{z_1 - z_2}{\lambda_{att}} \quad . \tag{23}$$

If z_1 and z_2 are the distances from the position of A_0 to the fiber's ends, the sum of z_1 and z_2 is the length L_{fiber} of the fiber.

$$z_1 + z_2 = L_{fiber} \tag{24}$$

$$z_2 = L_{fiber} - z_1 \tag{25}$$

Combining (25) with (23) allows to calculate z_1:

$$ln\left(\frac{A_1}{A_2}\right) = -\frac{2z_1 - L_{fiber}}{\lambda_{att}} \tag{26}$$

$$\Longrightarrow z_1 = -\frac{1}{2} \cdot \left(\lambda_{att} \cdot \ln\left(\frac{A_1}{A_2}\right) - L_{fiber}\right) \quad . \tag{27}$$

With (27) we found x_1, i.e. the position of A_0 from one of the fiber's endings. The plot of $\ln \frac{A_1}{A_2}$ versus z is a straight line with negative slope according to (27).
A BLM based on scintillation in scintillating fibers was tested at PITZ. The setup and results are presented in Sec. 5 and Sec. 5.4. The straight line with negative slope derived from the measurements is shown in Fig. 35.

5 Measurements with scintillating fibers

Originally it was planned to measure solely at PITZ. Unfortunately PITZ was temporarily not operationable, due to severe vacuum problems. Therefore, measurements were performed in laboratory using a ^{106}Ru source and at the proton ring accelerator DESY3 at DESY in Hamburg as well. These measurements are described in the Sec. 5.2 and 5.3. The measurements that were done at PITZ before the vacuum leak interrupted usual operation, will not be presented in this work. These were first experiences with the experimental setup and operation at PITZ, yielding for example to the conclusion that the distance between the PMs and the beam line has to be at least 80 cm. The ability to estimate the position of a beam loss with scintillating fibers is shown in Sec. 5.4.1. Some constraints on the results and fiber BLMs in general are discussed in Sec. 6.

5.1 The experimental setup

The experimental setup of the beam loss monitor using scintillating fibers was improved several times. Two slightly different setups differ in the kind of scintillator fibers chosen and will be described in this chapter.

The main concept is, to connect the scintillating fiber with optical fibers on both ends

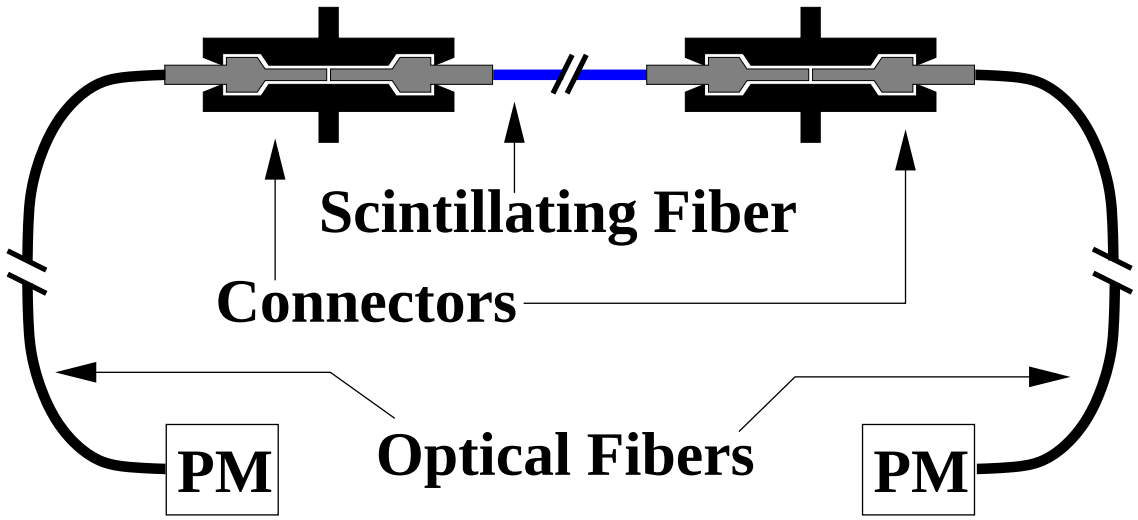

Figure 13: Sketch of the experimental setup. The scintillation fiber was mounted parallel to the beam tube.

which are read out by Photo Multipliers (PMs). The gluing of the scintillating fibers to optical fibers was dismissed in favor of commercial connectors (see Fig. 14) of the company *tyco electronics*[3]. This was motivated by the experience, that the scintillating fibers needed to be dismounted from the beam line several times. The connectors introduce an additional attenuation of the signal, because the boundary layers of the fibers are separated by thin air gaps in these connectors. These connectors, which are manufactured for fibers with 1.0 mm diameter, were drilled to fit the fiber's diameter. On both sides of the scintillating fibers, optical fibers guide the scintillation light to *Hamamatsu* Multianode

[3]see www.tycoelectronics.com: Part No. 228087-1 and 228042-1

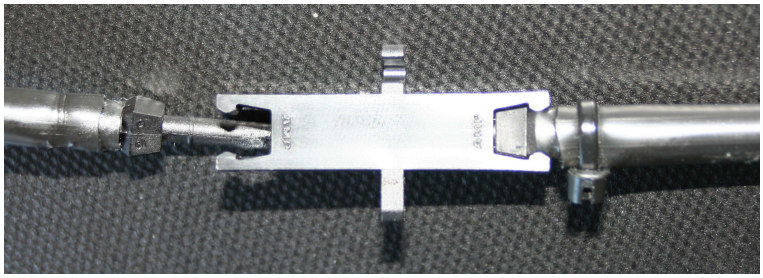

Figure 14: Photograph of one commercial connector used to connect optical and scintillating fibers.

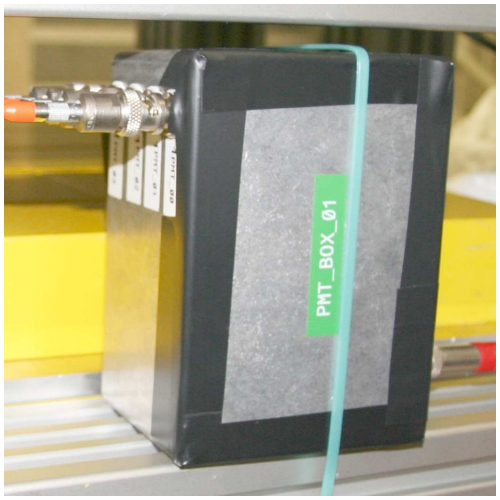

Figure 15: A PM box with black tape sealing. The four cables for the signal transport leave this box to the left side.

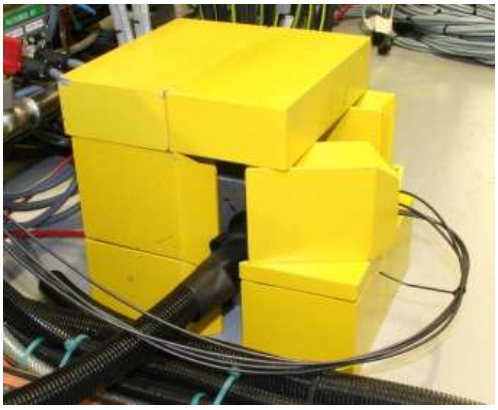

Figure 16: The PM box in additional shielding with lead bricks. The robust plastic tube protecting the optical fibers from mechanical damage can be seen entering the lead shielding.

Photomultiplier Tubes[4]. At a wavelength of 437 nm (481 nm) the PMs are supposed to have a quantum efficiency of 11 % (10.4 %) [30]. The optical fibers have a length of 2 m between the scintillating fibers and the PM. A mask is adjusting the optical fibers to point on the four pixels of the PMs, which are mounted in an iron box. Having 4 pixel at each PM, allows to read out different fibers. This makes test measurements easier and will be needed to estimate the transverse position of the beam loss in the future (see Sec. 4.1). The anode uniformity amongst the 4 pixel is specified by the manufacturer with maximum deviation of 18 %, the cross talk within 1.3 % [30].

For the read out, the signal was taken directly from the anode of the PMs without intermediate electronics and transmitted along approximately 2 m of coaxial cable [43] and approximately 45 m of N-type triaxicial cable [19] to the Control Room (CR) of PITZ. Here the signals were digitized and displayed by a Tektronix TDS5104B Digital Phosphor Oscilloscope. Most measurements presented in this work were done using the measurement function of this scope.

The scintillating fibers were supported by plastic rods (Fig 19). Doing this has several advantages:

[4]type: R5900U-00-M4 [30]

	scintillator	WLS	optical fiber
manufacturer	Kuraray	POL.HI.TECH.	POL.HI.TECH.
type	SCSF-81M	POLIFI S248-150	POLIFI 2-OP
diameter	480 μm	1.5 mm	1.5 mm
core material	polystyrene	unknown	unknown
$\lambda_{absorption}$	unknown	420 nm	unknown
$\lambda_{emission}$	437 nm	481 nm	unknown
λ_{att}	$\approx$ 2.5 m	unknown	$\approx$ 5 m

Table 4: Properties of the fibers. $\lambda_{emission}$ is the peak maximum of the emission wavelength spectrum, correspondingly $\lambda_{absorption}$. WLS stands for Wave Length Shifter and λ_{att} for attenuation length.

- the fibers are better protected from folding or other mechanical damage,
- the distance of the fiber to the beam tube is more close to be constant,
- storing the fiber (if unmounted) is done in a straight line not in circles; this prevents the plastic tube from additional folds which may hurt the fiber.

A disadvantage arising from the plastic rods is, that the distance from the beam line has to be enlarged up to 12 cm. Without rods, the fibers can be adopted to the beam lines shape.

5.1.1 Properties of the fibers

An important property of fibers transporting light is the attenuation of light along its path through the fiber. The attenuation length λ_{att} is a measure for the distance, over which the original intensity I_0 is attenuated to 1/e $\approx$ 37 % [50]. Amongst others, the attenuation length depends on the wavelength of the transported light, the index of refraction of the fiber and its cladding. The cladding is a thin layer of a special material that supports the total reflection of light inside the fiber.
Different scintillating fibers were used. One setup was a bundle of seven fibers of 480 μm each. These are *Kuraray*[5] SCSF-81M and were delivered to DESY in 1998 on spool.
WaveLength Shifting (WLS) fibers of 1.5 mm diameter from the company *POL.HI.TECH.* [41] were used as well. They were delivered to DESY in November 1996. The WLS fiber was used as scintillating fiber emitting light with 481 nm. A WLS fiber has a longer attenuation length than pure scintillation fibers. The optical fibers were manufactured by POL.HI.TECH. too and delivered to DESY in Feb. 1997.
Unfortunately is was not possible to find out more properties of the POL.HI.TECH. fibers than summarized in Tab. 4.
Due to the age of all these fibers, aging and therefore deviations of the referred values can not be excluded. Measurements investigating the effect of aging on these fibers were not done and publications investigating the aging without irradiation where not found. The fibers were stored in the cellar of DESY in Zeuthen. Aging can be tolerated if it results in

[5] www.kuraray.de

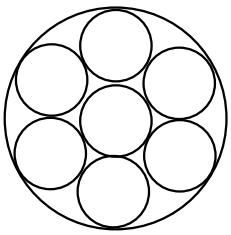

Figure 17: Seven circles of approximately 0.48 mm in one circle of 1.5 mm

Figure 18: The connectors wrapped in black tape. In the background the housing of an ICT is visible.

Figure 19: These plastic rods support the fibers whose flexible plastic tube is stuck to the opposite side of the rods.

homogenous changes for the whole fiber. The storing in the cellar should assure this.
For the measurements a 385 cm long WLS fiber from POL.HI.TECH. and 300 cm long fiber bundles of Kuraray SCSF-81M were prepared. The WLS fiber is composed of two fibers glued to each other. This introduces an additional attenuation at one position of the fiber in the order of 5 % [4].

5.1.2 Comparing bundle of thin fibers to single fiber

Using a set of thin fibers instead of one single fiber leads to a less sensitive detector, because the volume of the fiber bundle is just smaller than the volume of the single fiber. A rough estimation is given by the ratio of the volumes $\frac{V_{7\cdot 0.48mm}}{V_{1.5mm}} \approx 0.72$. The sensitive volume of the fiber bundle is just 72 % of the massive fibers volume.
One advantage arises from the fact, that the thin fibers are less fragile than a single fiber. In addition, the breakup of one thin fiber can at most reduce the amount of light traveling to the PM by 1/7 whereas the breakup of the single fiber at one position means a complete loss of all light for one PM of the detector.
The cross section area of the seven 480 μm fibers fits geometrically to the cross section area of a 1.5 mm fiber as visualized in figure 17. From this point of view, the coupling to the optical fibers is no problem.

5.1.3 Shielding of fibers and PMs

The experimental setup is shielded against visible light with several methods. The scintillating and optical fibers are placed in flexible light tight plastic tubes. In addition the set of four optical fibers was joined in a robust plastic tube on their way from the scintillating fibers to the PMs (see Fig. 16). The connectors between optical and scintillating fibers are supposed to be almost light tight but anyway they were wrapped in black tape in addition (Fig. 18). The PM boxes were also sealed up with black tape at the opening (Fig. 15).
In the presence of high background (see Sec. 5.3) the PMs need to be shielded against photons and electrons originating directly from interaction of the beam with the beam tube wall. Although it is unknown, if additional shielding with lead bricks is needed at PITZ, it was applied (see Fig. 16).

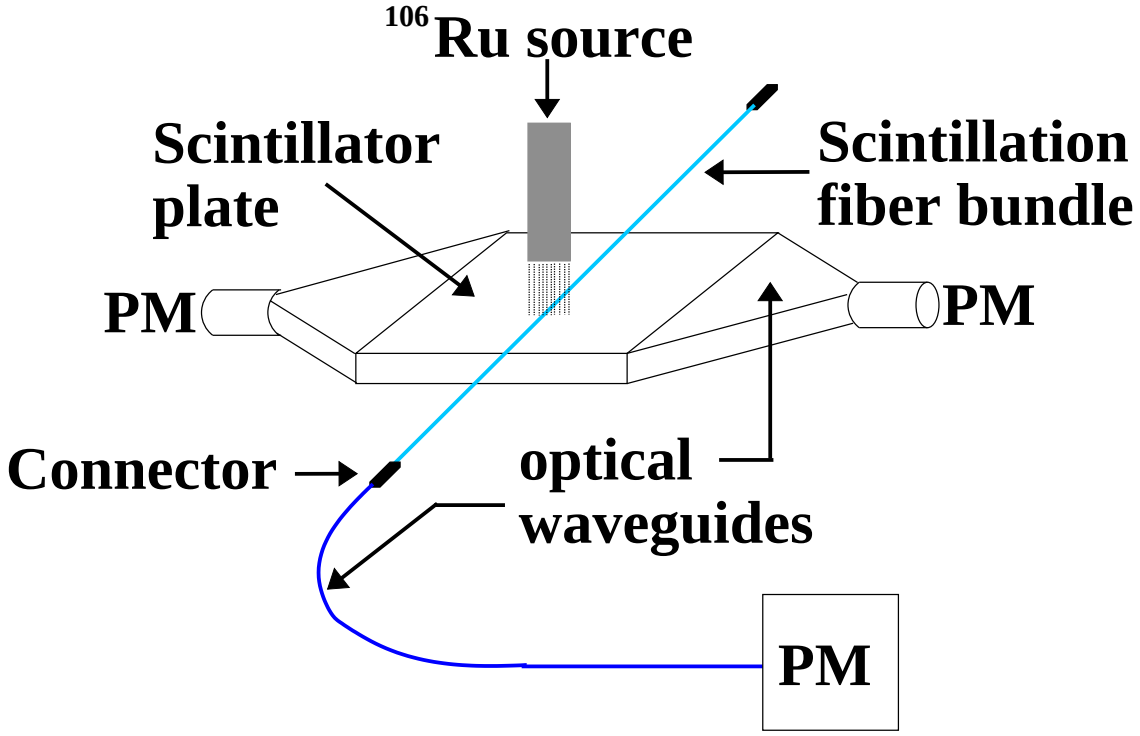

Figure 20: Sketch of the experimental setup looking for the coincidence of three PM signals. The scintillator plate had dimensions of approximately 10 cm x 10 cm x 1 cm.

5.2 Measurements with a ^{106}Ru source

The measurements with a ^{106}Ru source were performed, because PITZ was not operationable due to severe vacuum problems for several month. Using the Ruthenium instead of PITZ as electron source, investigations on the attenuation length of the scintillating fibers as well as the prediction of signal height and charge were planned.
^{106}Ruthenium is a β^- radiator. It has a half-life of $(366.6 \pm 0.9)d$ and the electron emitted has an energy of $(39.2 \pm 0.3)keV$.[6] The product of interest of the decay

$$^{106}Ru \longrightarrow {}^{106}Rh + e^- + \bar{\nu}_e \tag{28}$$

is not the electron but ^{106}Rhodium. The electrons produced in the decay of the ^{106}Rhodium are more significant. They were found by D.E. Alburger [2] to have energies of $(3.53 \pm 0.01)\ MeV$ (68%), $(3.1 \pm 0.1)MeV$ (11%) and lower. The half-life of Rhodium is in the order of few seconds and therefore not important for this experiment.
The ^{106}Ruthenium source used, is a sealed radioactive source[7]. The certificate[8] specified a nominal activity of 4 MBq on th 18th March 2004. As the measurements with this source where done in March 2006, an activity of roughly 1 MBq was available.
A fiber bundle (seven fibers of $480\mu m$, see Tab. 4) was set up in laboratory along a table and connected via optical fiber to a PM. An increase of counting rate was observed when exposing the fiber bundle to the source. Yet, unstable perturbations of unknown origin eliminated the possibility to relate specific signals to the Ruthenium source. To correlate

[6] see [35], p.376f
[7] a so called *Demonstrationsstrahler*
[8] no. 71616 - MG 348, AEA Technology QSA GmbH (Braunschweig-Germany)

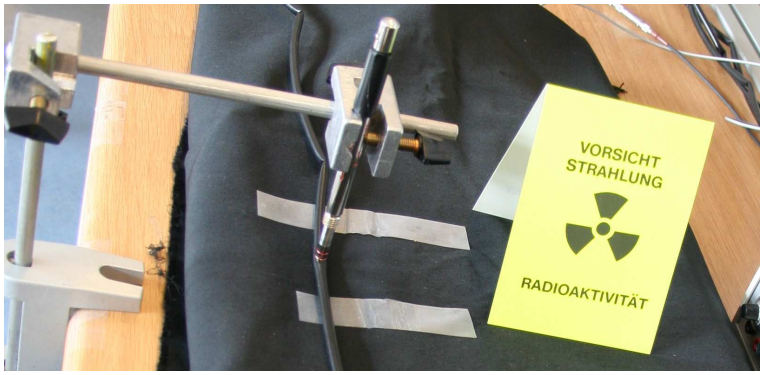

Figure 21: Experimental setup for the measurements with ^{106}Ru. The cloth covering the fibers was removed for the photograph.

the observed signals, a trigger based on the coincidence of three signals was build up. For this purpose, a plate of scintillator was placed beneath the fiber. The scintillation fiber bundle and the scintillator plate were enwrapped in black cloth and black plastic foil. From the top, the Ruthenium source was fixed with support material pointing on the fiber bundle and the plate beneath. The scintillator plate was read out from two PMs (Fig. 20). The signals from the three PMs were transformed to rectangular pulses using a NIM discriminator[9]. These three rectangular pulses were connected to a NIM coincidence unit[10] and their coincidence was used as trigger pulse for an oscilloscope. The signals observed using this trigger were not stable.
Apart from the problems to identify pulses originating from the Ruthenium source, the increase of the signal rate was obvious. A NIM counting unit[11] was used to count the number of coincidences of the three rectangular pulses originating from the three PMs. Shifting the support material with the Ruthenium source and the plate enabled different positions of irradiation along the fiber bundle and therefore different travelling length of the scintillation light through the scintillation fibers of the bundle. A series of measurements was done to estimate the attenuation length λ_{att} of the scintillation fibers.
The fluctuations of the observed counting rates were tremendous.

Fig. 22 gives an impression of these fluctuations. The temporal stability of the number of coincidences from the three PMs is shown there. These measurements were performed at fixed position of the ^{106}Ru source relative to the fibers and without long temporal gaps between the measurements. Similar fluctuations were observed at other positions.
A β^- source with $A = 1MBq$ activity coming through the circular opening (Ø 7 mm) of the sealed source is the equivalent of the fluence Φ_{e^-} of

$$\Phi_{e^-} = \frac{A}{area} \approx 26 \cdot 10^3 mm^{-2} s^{-1} \quad . \tag{29}$$

Looking only for electrons above 3 MeV the fluence has to be reduced to 79 % according to Alburger [2]. So a fluence of $\Phi_{e^-} \approx 21 \cdot 10^3 mm^{-2} s^{-1}$ has to be taken into account. Let 6 mm of each fiber be directly irradiated by the source. This assumption results in an effective area of $A_{fibers} = 7 \cdot 6mm \cdot 0.48mm = 20.16mm^2$ of the irradiated scintillator. The

[9]CAEN, 4 Channel discriminator, mod. 84
[10]CAEN, QUAD Coincidence Logic Unit, mod. N455
[11]CAEN, QUAD Scaler and Preset Counter, mod. N145

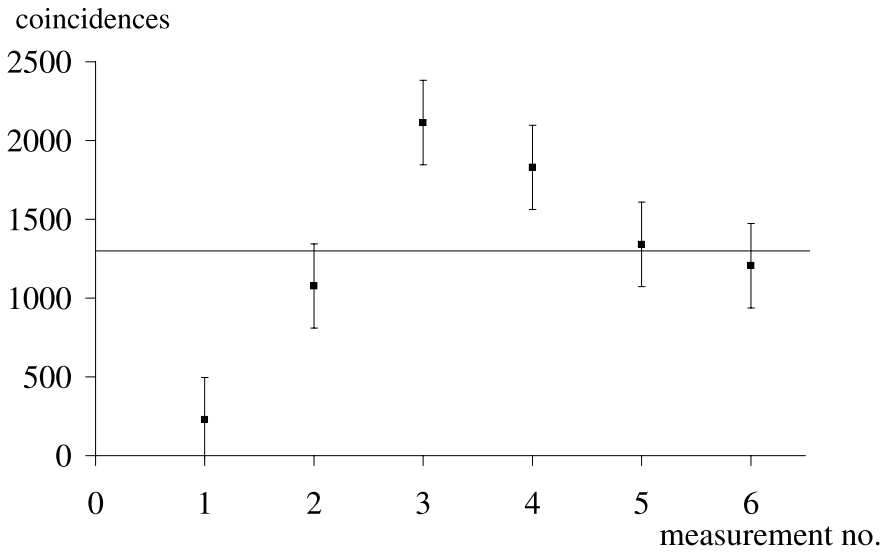

Figure 22: Test of signal stability at 80 cm distance from the optical fibers. Each measurement was counting all coincidences from the three signals for 600 seconds.

product of the fluence Φ_{e^-} and the area A_{fibers} gives the rate

$$r_{e^-} \approx 4 \cdot 10^5 s^{-1} \tag{30}$$

of electrons passing through the fibers.
The cosmic muon background has to be taken into account. Considering only cosmic muons from above, [15] announces a flux of $\Phi_\mu = 130 \cdot m^{-2}s^{-1} = 1.3 \cdot 10^{-2}\ cm^{-2}s^{-1}$ while [3] gives $\Phi_\mu = (1.44 \pm 0.09) \cdot 10^{-2}\ cm^{-2}s^{-1}$. For a rough estimation of the muon background [3] will be used. The seven fibers of 480 μm on the scintillator plate with a length of 10 cm cover an area of

$$A_{fibers\ on\ plate} = A_{fop} = 10cm \cdot 7 \cdot 0.048cm = 3.36cm^2 \quad . \tag{31}$$

This results in a muon rate of

$$r_\mu = \Phi_\mu \cdot A_{fop} = (4.8 \pm 0.3) \cdot 10^{-2}\ s^{-1} \quad . \tag{32}$$

The 3 MeV electrons of the ^{106}Ru source have a mean energy loss of $\frac{dE}{dx}\big|_{e^-} \approx 1.883 \frac{MeV}{cm}$ in polystyrene [21]. This nearly equals the energy loss of the muons $\frac{dE}{dx}\big|_{\mu} \approx 1.998 \frac{MeV}{cm}$ [21]. With almost equal energy loss but seven orders of magnitude difference in the rate, the cosmic background can not be the origin of the fluctuations. Further investigations on the source of these fluctuations were aborted in favor of measurements at the proton accelerator ring DESY3.

5.3 Measurements at the DESY3 proton ring accelerator

At DESY in Hamburg the facility DESY3 is a ring accelerating protons with a ramp of 4.7 GeV/s up to a momentum of 7.5 GeV/c. There are 11 bunches with approximately 10^{11} protons per bunch in one injection cycle.
At the beginning of the ramping the proton bunches, which are very broad and almost adopt the complete tube diameter, are following each other nearly continuously along the ring. Increasing energy leads to a compression of the bunches and rising temporal gaps between them.
The ramping from 0.3 GeV/c to 7.5 GeV/c takes approximately 1.6 seconds and is suc-

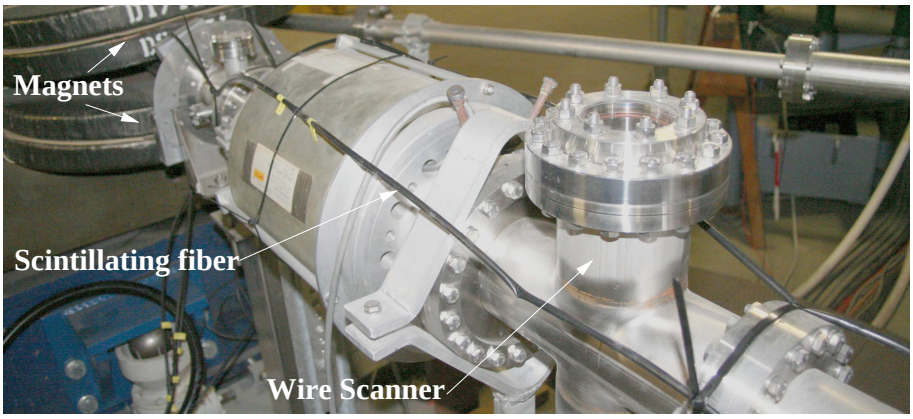

Figure 23: The experimental setup at the DESY3 proton ring.

ceeded by a flat top of approximately 0.6 seconds at 7.5 GeV/c. The proton bunches are then ejected to PETRA[12] and from there injected to HERA[13] for further acceleration and collision with electrons.
At a certain position of DESY3, a Wirescanner is mounted and used for tests of beam diagnostics. This wire is different from the one described in Sec. 2. Here, a 7 μm graphite wire is used. Although the shower produced by protons in the wire or the iron tube walls is mainly hadronic, it includes an electromagnetic component originating for example from the decay of charged pions (see [10] for example).
Unfortunately a bending magnet was following behind the Wirescanner in a distance of lower than 1 m (Fig. 23). Considering the energy of the protons, it is rather improbable that a great fraction of the secondary particles produced by the wire find their way to the fibers before entering the magnet. Anyway, there should be much electrons around the beam tube, as the beam is very broad and interaction with the tube wall results in secondary particles too.

A FLUKA simulation was applied to estimate the expected amount of electrons (see Fig. 26, 27 and 28). The geometry was implemented to include an iron tube (Ø 2.0 cm), the graphite wire (at z = 50 cm) and four scintillation fibers of Ø = 1.5 mm made of polystyrene (see Appendix A). The polystyrene fibers were placed in a distance of 3 cm from the beam axis. The protons had a momentum of 7.5 GeV/c and were Gaussian distributed with $\sigma = 2mm$. The shower produced by the wire of the Wirescannner contributes very little to the deposited energy in the fibers according to this simulation. The

[12]Positron Elektron Tandem Ring Anlage
[13]Hadron Electron Ring Accelerator facility

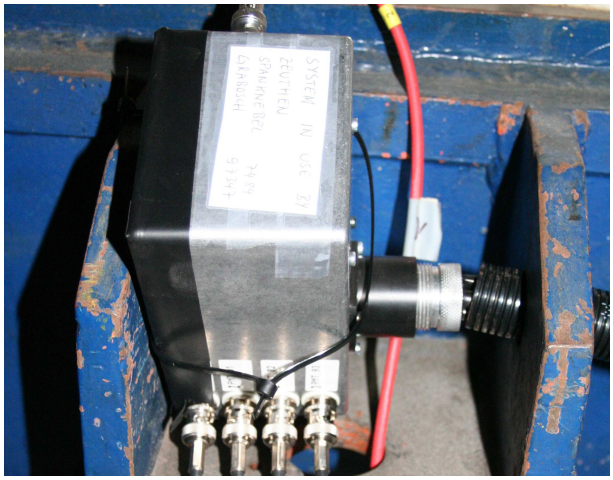

Figure 24: PM in the DESY3 tunnel.

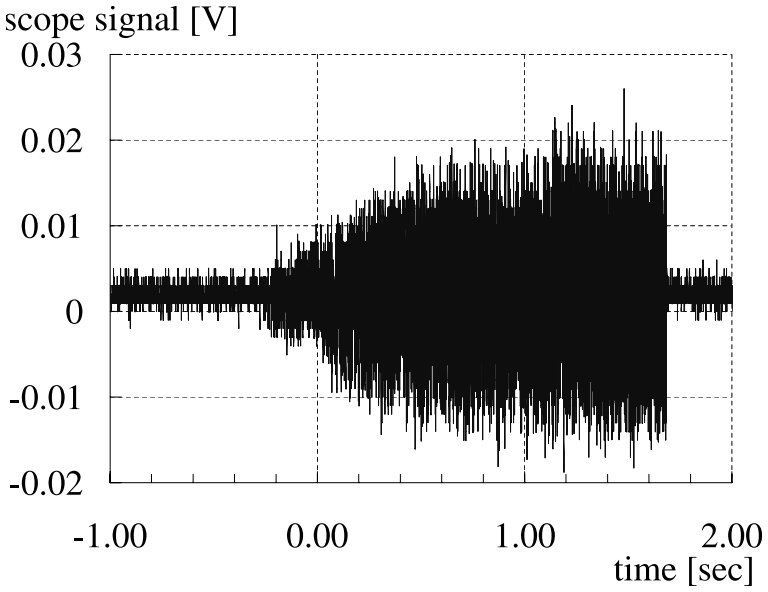

Figure 25: Scope signal of one injection cycle.

proton beam was started at z = 3 cm. The main contribution to energy deposition in the fibers is caused by particles produced by the interaction of the protons with the tube wall (see Fig. 28).
The fibers were mounted along a short part of the beam tube including the WS station (Fig. 23). The PMs were put to the ground behind some iron parts of the support frame of the following magnet (Fig. 24). It turned out, that this shielding was not enough. The signal recorded (Fig. 25) when the optical fibers were disconnected from the PM (i.e. the PM should be 'blind') was not different from the signal with optical fibers and scintillating fibers connected. As expected, the influence of the wire being 'in' or 'out' of the beam was not visible.
DESY3 was a strong demand on the need of proper shielding for the PMs. The following measurements at PITZ where done with additional lead brick shielding (see Fig. 16).

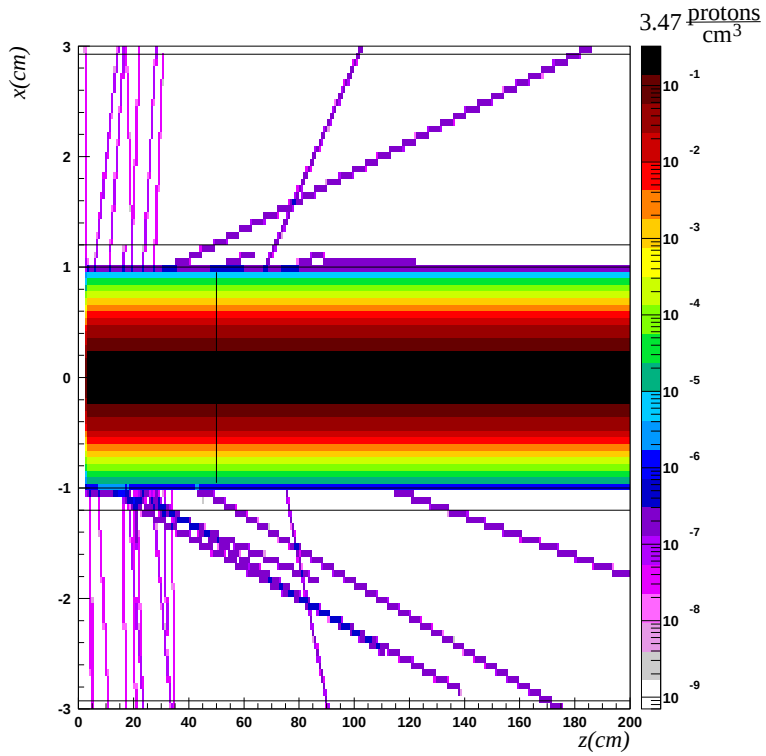

Figure 26: Plot of a FLUKA simulation showing the proton density per incident proton. The wire of the Wirescanner is visible at z = 50 cm. The fibers are visible at x = $\pm$ 3 cm parallel to the beam tube.

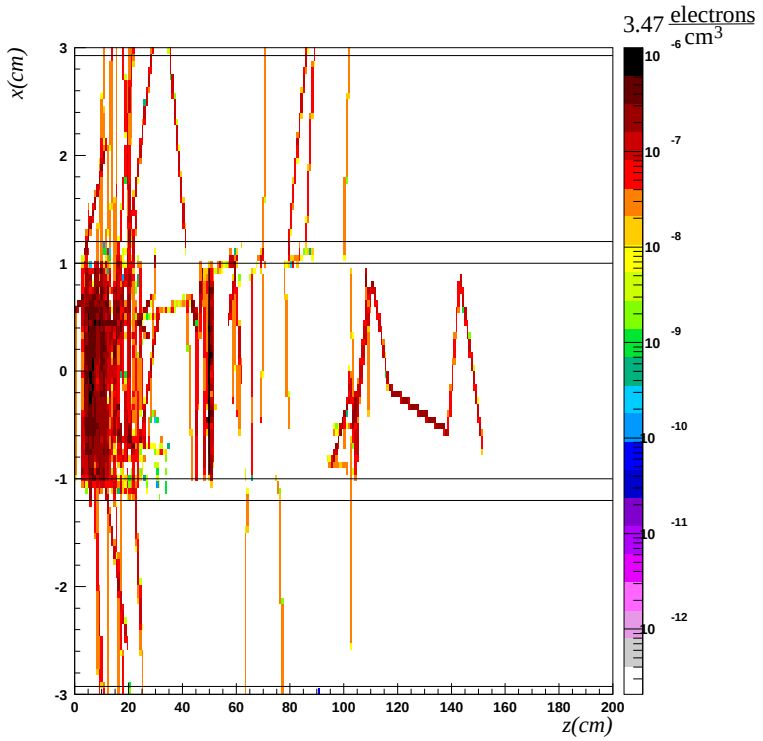

Figure 27: Electron density per incident proton (same simulation as Fig. 26). Most electrons are produced shortly after the z = 3 cm, where the proton beam started in this simulation.

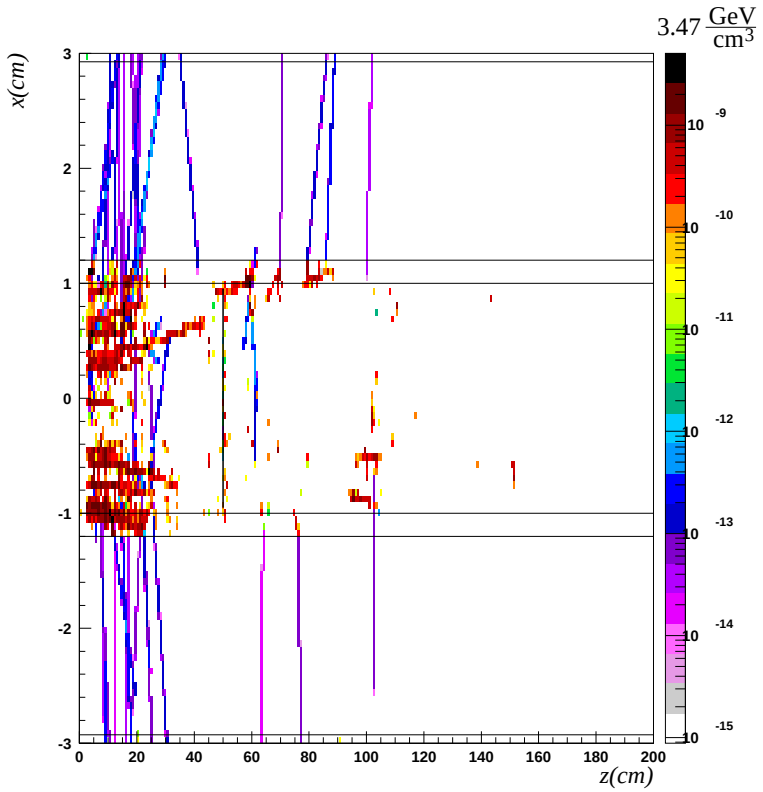

Figure 28: Density of energy deposition per incident proton (same simulation as Fig. 26).

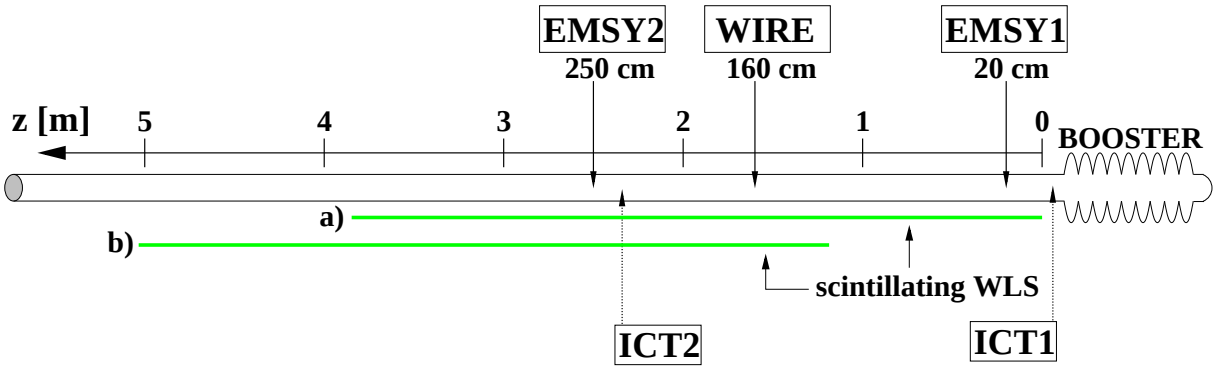

Figure 29: Longitudinal positions of the scintillating fibers at PITZ. The scintillating WLS was shifted once from *a)* to *b)* with the fiber starting at z = 120 cm in configuration *b)*. Note, that z = 0 cm is the beginning of the fibers in configuration *a)*, not the beginning of the beam line. The absolute positions relative to the cathode surface can be derived with Tab. 1. The ICTs are situated before EMSY1 and before EMSY2 (see also Tab. 1).

5.4 Measurements at PITZ

The measurements at PITZ were done in July 2006 at PITZ (status after second upgrade) and are all based on a WLS fiber with 1.5 mm diameter (see Tab. 4). The fiber was supported by a plastic rod (see Fig. 19) and mounted almost parallel to the beam axis in a distance of approximately 12 cm. After the BOOSTER, the electrons had an energy of approximately 12 MeV. Fig. 29 shows two different settings of z-positions for the fiber. Steering the beam into the beam tubes wall at a precise position would be difficult and hardly reproducible. Instead the EMSY slit masks and the wire of the Wirescanner are used to produce showers which have a known origin and are easily reproducible. The z-position of these devices is used w.r.t. the beginning of the WLS fiber in configuration *a)*. As visible in Fig. 2, other screens (HIGH1.Scr2 and HIGH1.Scr5) could have been used as well. Due to unknown material and material thickness of these screens, this was abandoned.
Typical signals at the scope are shown for the Wirescanner in Fig. 30 and for the EMSY1 in Fig. 31. In these screenshots from the scope, the magenta signal belongs to ICT1 (see Fig. 29 and Tab. 1) the green signal to ICT2. The yellow signal (Ch1 of the scope) is the signal from the WLS fiber in upstream direction, the blue signal (Ch2) from the WLS fiber in downstream direction. The PITZ master-trigger was used.
GEANT simulations were applied to understand the signals. A vacuum filled iron tube was implemented and surrounded by 4 polystyrene (see Appendix A) fibers of 1.5 mm diameter. An electron beam was directed to a 1.0 mm plate of tungsten. The electrons were Gaussian distributed with a σ of 0.2 mm and given the momentum of 12 MeV/c. The deposited energy in the fibers was scored and averaged yielding to $(0.193 \pm 0.03)\, keV$ per incident electron. Similar results were obtained with FLUKA.
From the ICT signal in Fig. 31 a charge of 0.98 nC was detected. This amount was incident to the tungsten slit mask. Extrapolating the simulation data to the measured charge, a total deposited energy of $(1170 \pm 20)\, GeV$ is estimated. The effects considered for signal transport and processing are summarized in Tab. 5. Taking these into account ends up in a predicted charge at the scope of $(93 \pm 42)\, nC$. This differs from the measured $(0.23 \pm 0.02)\, nC$ by more than two orders of magnitude. Although the effects listed in

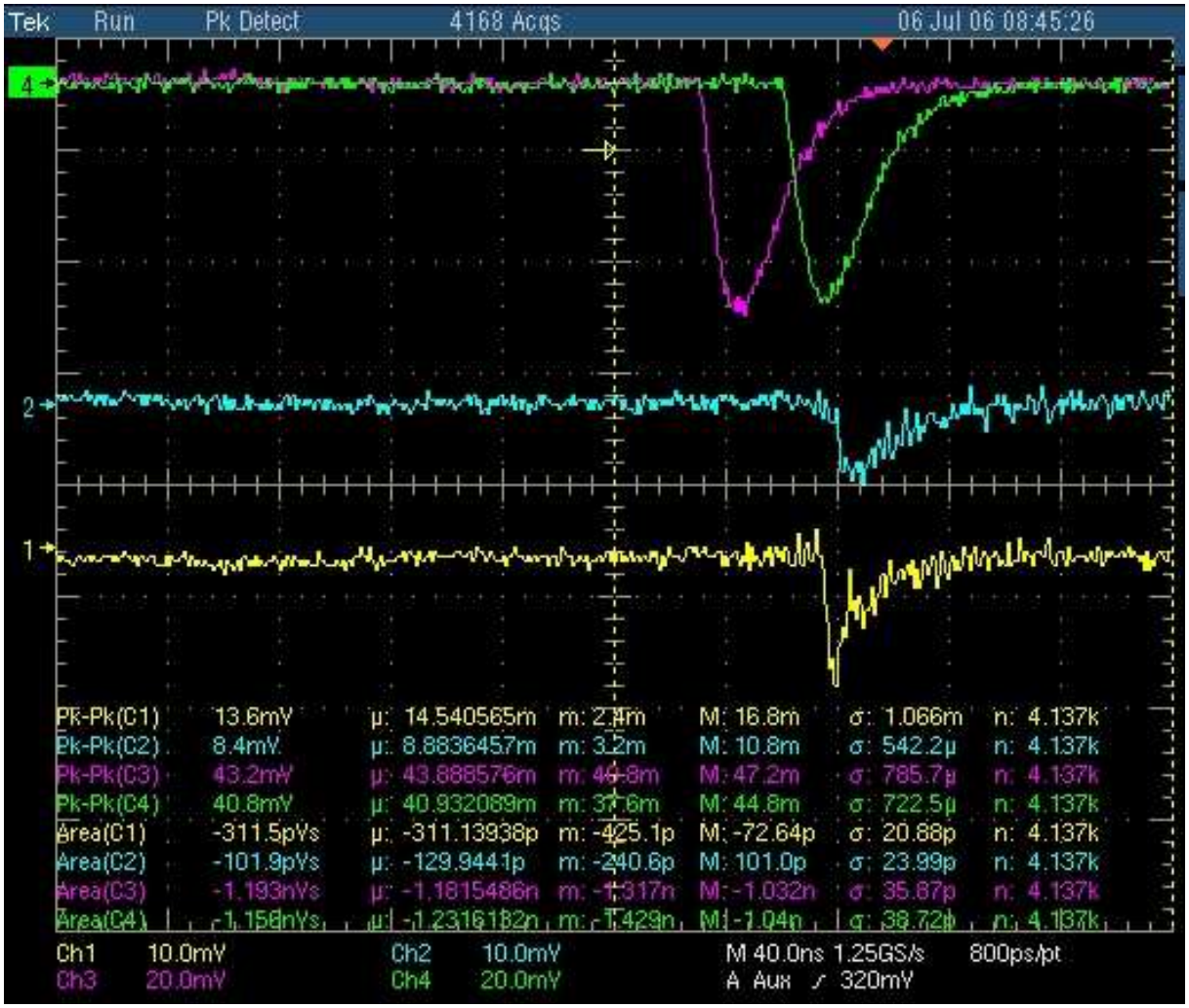

Figure 30: Signals from the WLS fiber displayed on the digital scope in configuration *a)*. The yellow and the blue signal are from the different ends of the fiber. Magenta and green belong to ICT1 and ICT2 (see Fig. 29). The wire of the Wirescanner was inserted at this measurement. The signal from ICT2 (green) is a little bit smaller than that from ICT1 (magenta). This indicates, that only few electrons of the bunch interacted with the wire and are not detected by ICT2. The signal from the upstream side of the fiber (Ch1) is slightly bigger than that from the downstream side (Ch2). Considering that the shower initiated by the wire passes the fiber before it's middle, the signal ratio is reasonable. For each channel the *peak to peak* (pk-pk) voltage and the area included by the signal is measured. These measurements are done between the cursors (indicated by dashed vertical lines: one in the middle, the other at the right border) and displayed on the screen. The mean (μ) and the standard deviation (σ) are calculated based on the last 32 measurements and displayed. In addition the minimum (m) and maximum (M) value is shown.

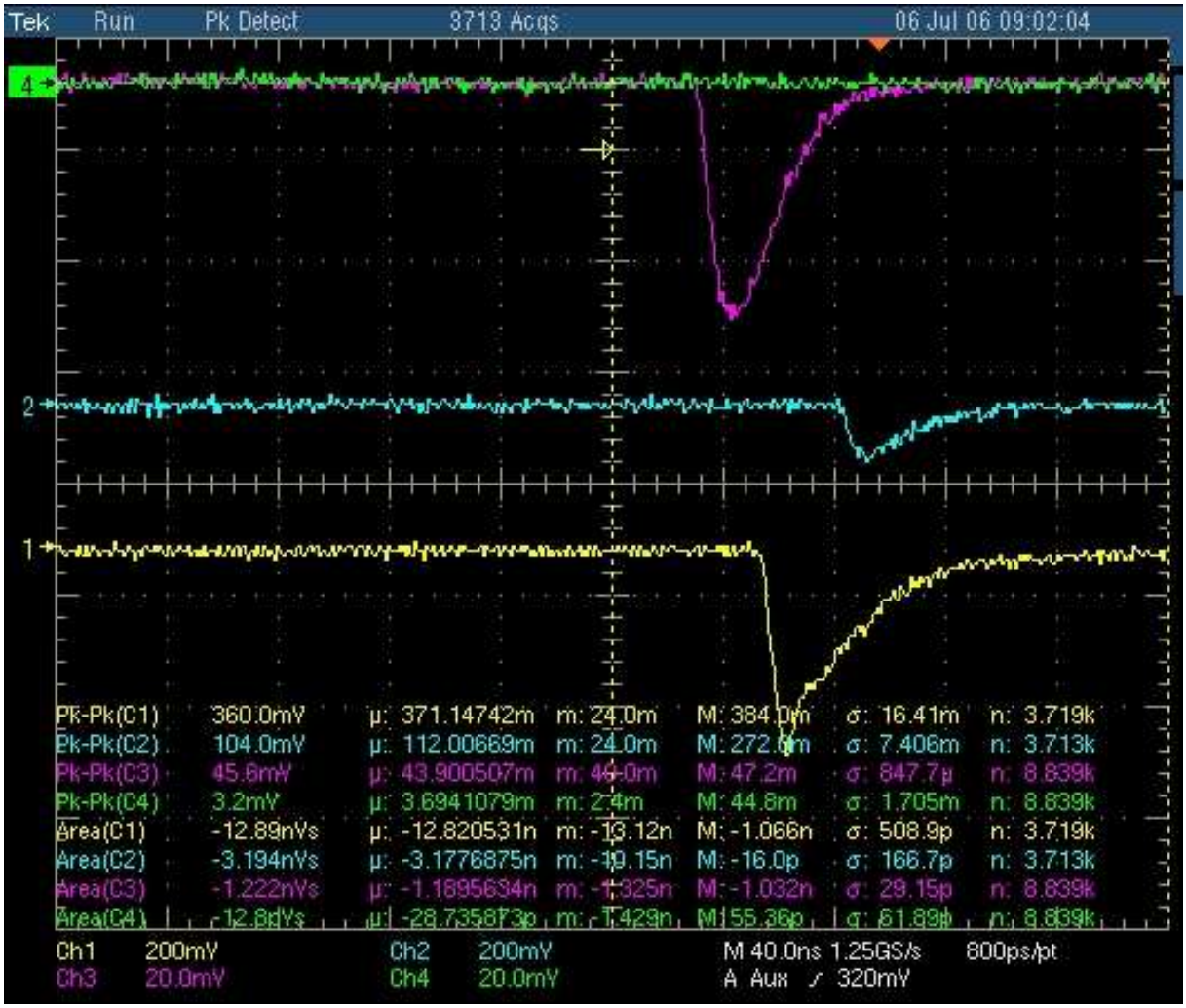

Figure 31: Here the tungsten slit mask of EMSY1 was inserted to the beam line between the ICT1 and ICT2 in configuration *a)*. ICT2 detects almost no charge because the charge is mainly absorbed in the tungsten mask of EMSY1 and the beam tube. The signals from the WLS fiber are much higher than the signals obtained when the Wirescanner was inserted (Fig. 30). EMSY1 is situated at the beginning of the fiber. Hence the signal of Ch1 is much bigger than that of Ch2. The different runtime of the signals Ch1 and Ch2 is approximately 28 ns. Using a pulse generator the difference in the runtime of the signals due to different cable length was measured to be $\Delta t_{cable} \approx 9.0ns$ (Ch1 9 ns before Ch2). In Sec. 5.4.1 we will learn, that the energy deposition from EMSY1 is located 22 cm behind the beginning of the scintillating fiber. Hence, the different runtime of the scintillation light in the fiber is $\Delta t_{fiber} = \frac{\Delta s}{v_{light}} = \frac{385cm-2 \cdot 22cm}{c/n} = \frac{3.41m \cdot 1.581}{3 \cdot 10^8 m} \cdot s = 18ns$. Here, Δs is the difference of travelling length in the fiber, c the speed of light in vacuum and n = 1.581 the refraction index of polystyrene [17]. The sum of Δt_{fiber} and Δt_{cable} is 27 ns and explains the observed temporal difference. In Fig. 30 approximately 8 ns between Ch1 and Ch2 are measured. Here, the longitudinal position of the energy deposition in the fiber is 181 cm (see Wirescanner in Sec. 5.4.1). Thus, the difference including the different cable length should be $\approx 10ns$, which is still a good estimation.

Table 5: Effects of signal transport and processing

considered effect	Value	unit	data source
light yield in scintillating fiber	8000	$\frac{\gamma}{MeV}$	[9]
trapping of photons in scint. fiber	4	%	[27]
attenuation length of the scint. fiber	3.1	m	Sec. 5.4.1
attenuation at the plugs to optical fibers	5	%	[4]
attenuation length of the optical fiber	5.0	m	[41]
attenuation at the interface to PM	20	%	educated guess
quantum efficiency of PM at 481 nm	0.104	$\frac{e^-}{\gamma}$	[30]
gain of PM at 400 V	10^4	-	[30]
attenuation along 45 m N-type cable	-2.2	dB	[19]

Tab. 5 are rather estimations (relative error of 50 %), the difference of two orders of magnitude is not understood.
Anyway, the S/N ratio is by far good enough to identify and count individual pulses easily, which will be necessary for the specification of intolerable beam losses. The signal height for real beam losses into the beam tube of PITZ should give even better signals. The prediction of signals using an experimentally adjusted conversion factor is one of the possible next steps to classify not only the number but also the quality of a beam loss belonging to a special scope signal.

5.4.1 Scintillating fibers for position estimation

The estimation of the position of a beam loss can be done by evaluating the $\ln\left(\frac{A_1}{A_2}\right)$ with A_1 and A_2 being the signal amplitudes of the scintillating fiber in upstream and downstream direction (see Sec. 4.4.3). If the signal transport and processing is equal for both signals, the ratio of the amplitudes at the fiber's ends equals the ratio of the signals measured with the scope. It was assured, that these conditions are fulfilled as good as possible. Some constraints are discussed in Sec. 6.
For these measurements, the two EMSY slit masks (EMSY1 and EMSY2) were subsequently inserted to the beam line (configuration *a)* in Fig. 29). FLUKA plots of the simulated electrons and the energy deposition are shown in Fig. 32 and 33. As only the ratio is considered, even the signals from the Wirescanner should match to this series of measurements and were recorded (configuration *a)* again). To obtain an additional point in the measurement series the scintillating WLS fiber was shifted in the PITZ tunnel. In this configuration *b)* the EMSY2 was at z = 135 cm.
A problem occurs when the measured amplitude ratios have to be assigned to z-positions. Here, the position of the energy deposition in the fiber has to be chosen as z-position. This information is experimentally difficult to access. Discrete BLMs of the company BERGOZ (see Sec. 4.3) were used to determine the position of the beam losses. Due to a lack of experience with these devices, the measurements did not succeed because the shielding was not sufficient. FLUKA and GEANT simulations were applied to determine the positions of the energy deposition into the fibers. The geometry was kept as described in Sec. 5.4 but the number of fibers was reduced to one.
The energy deposition in the fiber was counted including the longitudinal position in a

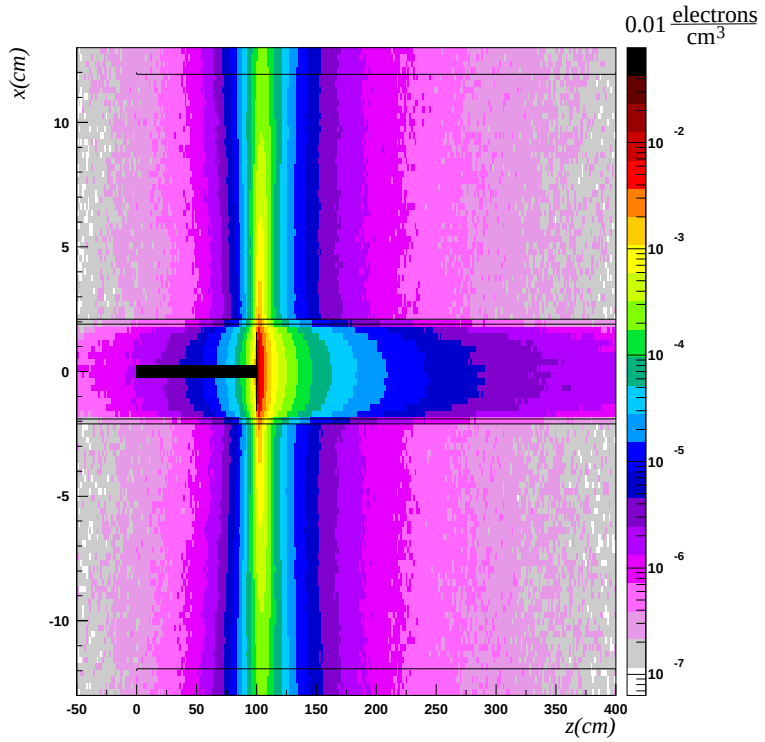

Figure 32: FLUKA plot showing the geometry and the electron density per incident 12 MeV electron.

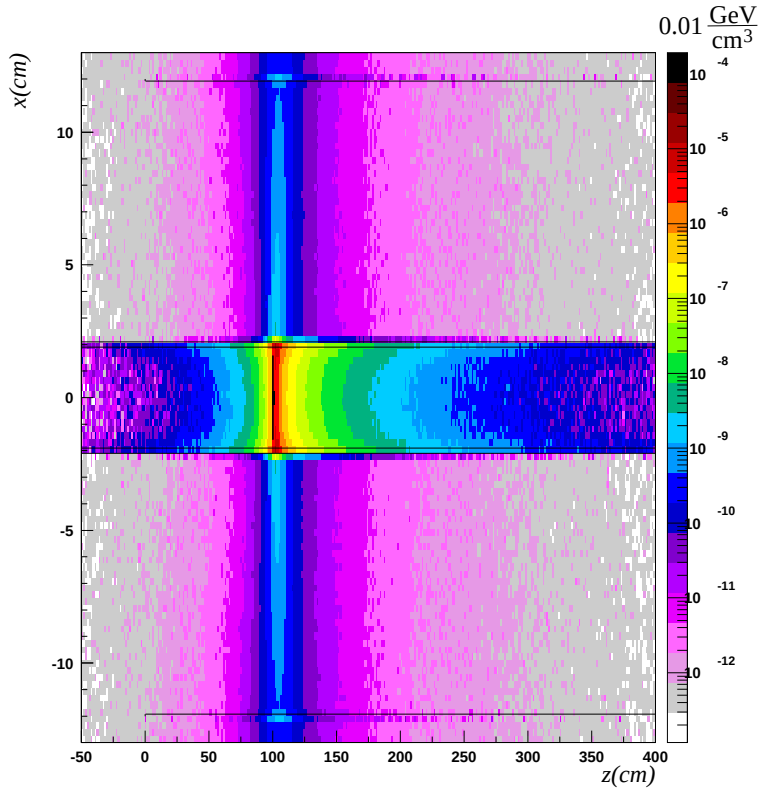

Figure 33: FLUKA plot showing the geometry and the density of deposited energy per incident 12 MeV electron.

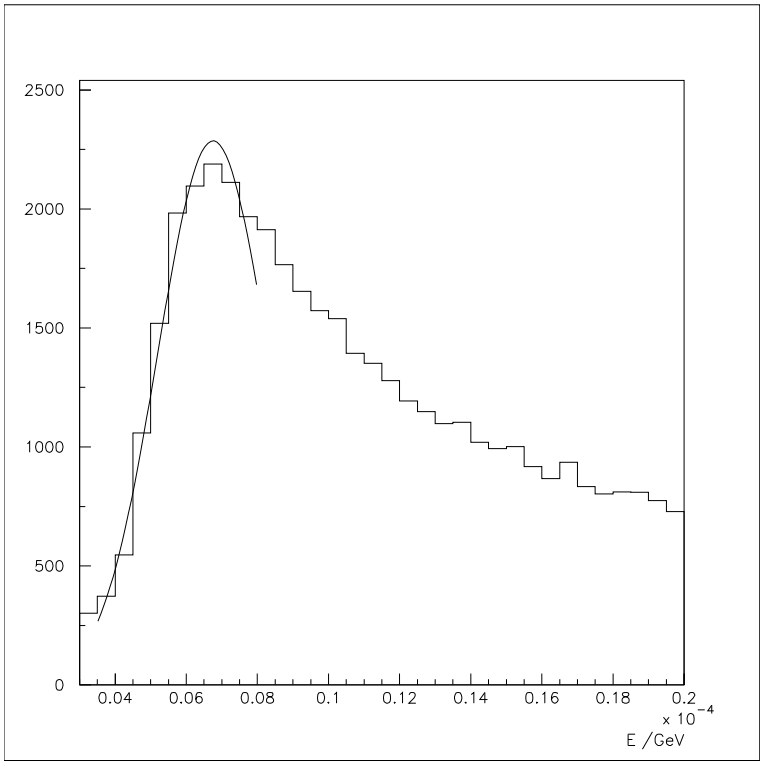

Figure 34: Histogram of the energy distribution at one end of the fiber.

histogram. The mean value and the error of the distribution of the energy along the fiber was calculated with the PAW [38] statistics option. The mean was taken as z-position of the energy deposition into the fiber yielding to $(2.4 \pm 7.3)\,cm$ distance between EMSY slit masks and the deposition maximum in the fiber. For the tungsten wire this distance is $(21.1 \pm 10.7)\,cm$. These displacements were used for the determination of z-positions for the measured *and* the simulated amplitude ratios and are listed in Tab. 6. The observed temporal difference between the upstream and downstream signal (see Fig. 31) can be explained applying these z-positions.

Whenever a particle lost energy in the fiber, energy deposition and the corresponding z-position were used to calculate the amount of energy arriving at the both ends of the fiber based on exponential attenuation according to

$$dE(z) = dE \cdot e^{-\frac{1}{\lambda_{att}} \cdot z} \quad . \tag{33}$$

The energies calculated for the fiber's ends were summed up on the one hand and scored in a histogram on the other hand. The histogram in Fig. 34 shows a part of the Landau distribution of energies retrieved from for one end of the fiber. Here a Gaussian fit was made to estimate the most probable energy $A_{sim,i}$ (i=1,2) and it's error $\sigma_{sim,i}$. The different $A_{sim,i}$ were then taken for the amplitude ratio. It turns out, that the ratio of the energies that were summed up is similar to that of the most probable energies $A_{sim,i}$. In Fig. 35 the logarithm of the for measured and simulated amplitude ratios is plotted versus the z position of the energy deposition in the fiber. The errors were propagated according to the laws of error propagation (see (35)) and are summarized together with the values in Tab. 7.

device	position of device [cm]	Δz [cm]	position of maximum in fiber [cm]	σ_{zpos} [cm]
EMSY1	20 ± 2	2.4 ± 7.3	22.4	7.6
EMSY2 *b)*	135 ± 2	2.4 ± 7.3	137.4	7.6
Wirescanner	160 ± 2	21.1 ± 10.7	181.1	10.9
EMSY2 *a)*	250 ± 2	2.4 ± 7.3	252.4	7.6

Table 6: Relative longitudinal positions of the devices inserted into the beam line (see Fig. 29) and their errors. Δz is the longitudinal distance between the position of the device and the simulated maximum of energy deposition in the fiber. The errors of Δz were retrieved from a Gaussian fit of the simulated distribution. The errors of the device position and Δz were propagated to the errors σ_{zpos} of the position of the maximum in the fiber.

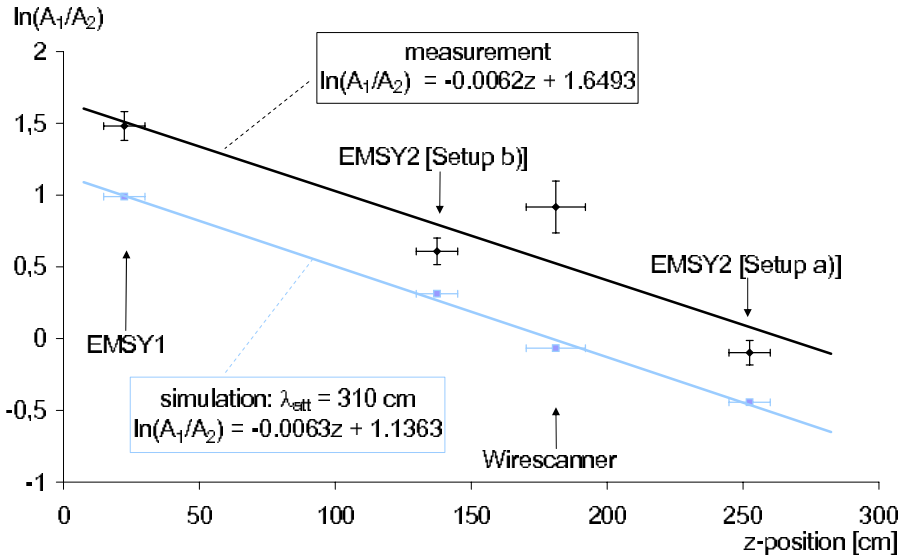

Figure 35: The logarithm of the amplitude ratios in dependence of the z-position of the energy deposition in the fiber.

measurements, κ = exp						
device	$A_{exp,1}$ [V]	$\sigma_{exp,1}$ [V]	$A_{exp,2}$ [V]	$\sigma_{exp,2}$ [V]	$\ln\left(\frac{A_{exp,1}}{A_{exp,2}}\right)$	$\sigma_{exp,ln}$
EMSY1	0.338	0.007	0.077	0.008	1.5	0.1
EMSY2 *b)*	0.167	0.008	0.091	0.007	0.61	0.09
Wirescanner	0.011	0.001	0.0044	0.0007	0.9	0.2
EMSY2 *a)*	0.104	0.006	0.115	0.007	-0.1	0.09
simulation with $\lambda_{att} = 310cm$, κ = sim						
device	$A_{sim,1}$ [keV]	$\sigma_{sim,1}$ [keV]	$A_{sim,2}$ [keV]	$\sigma_{sim,2}$ [keV]	$\ln\left(\frac{A_{sim,1}}{A_{sim,2}}\right)$	$\sigma_{sim,ln}$
EMSY1	10.01	0.01	3.722	0.003	0.99	0.001
EMSY2 *b)*	7.09	0.006	5.188	0.004	0.312	0.001
Wirescanner	5.93	0.01	6.34	0.01	-0.067	0.003
EMSY2 *a)*	4.79	0.004	7.465	0.006	-0.444	0.001

Table 7: Measured and simulated amplitudes used for Fig. 35.

The error $\sigma_{\kappa,ln}$ (κ = sim,exp) of the logarithm of the amplitude ratio is based on the observed standard deviations $\sigma_{\kappa,i}$ (i=1,2) of the amplitudes $A_{\kappa,1}$ (upstream direction) and $A_{\kappa,2}$ (downstream direction)

$$\sigma_{\kappa,ln} = \sqrt{\left(\sigma_{\kappa,1}\frac{\partial}{\partial A_{\kappa,1}}\ln\left(\frac{A_{\kappa,1}}{A_{\kappa,2}}\right)\right)^2 + \left(\sigma_{\kappa,2}\frac{\partial}{\partial A_{\kappa,2}}\ln\left(\frac{A_{\kappa,1}}{A_{\kappa,2}}\right)\right)^2} \tag{34}$$

$$= \sqrt{\left(\frac{\sigma_{\kappa,1}}{A_{\kappa,1}}\right)^2 + \left(-\frac{\sigma_{\kappa,2}}{A_{\kappa,2}}\right)^2} \quad . \tag{35}$$

By applying (33) to the measurements, an attenuation length of $(310 \pm 5)\,cm$ was found for the scintillating WLS fiber. The nominal attenuation length of the WLS fiber is not known (see Sec. 5.1.1), but 3.1 m seem to be realistic [41]. The difference between measured and simulated $\ln\left(\frac{A_{\kappa,1}}{A_{\kappa,2}}\right)$ can be cleared by applying a correction factor of $f_{corr} = 1.69$ to the measured amplitudes of PM2. PM1 (upstream direction) was operated at 470 V and PM2 (downstream direction) at 400 V. These values were chosen, because the amount of light from the WLS fiber caused saturation of the PMs if higher voltage was applied. A High-Voltage of 400 V is at the lower limit of the PM operation range [30]. The different

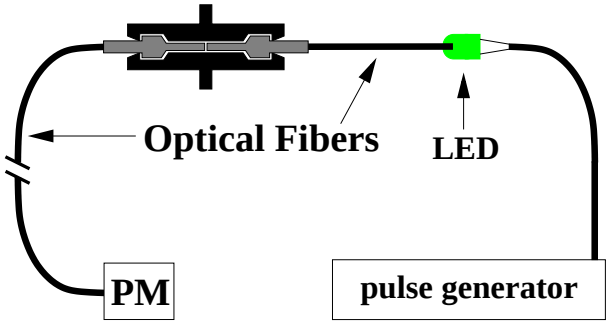

Figure 36: Experimental setup for PM calibration.

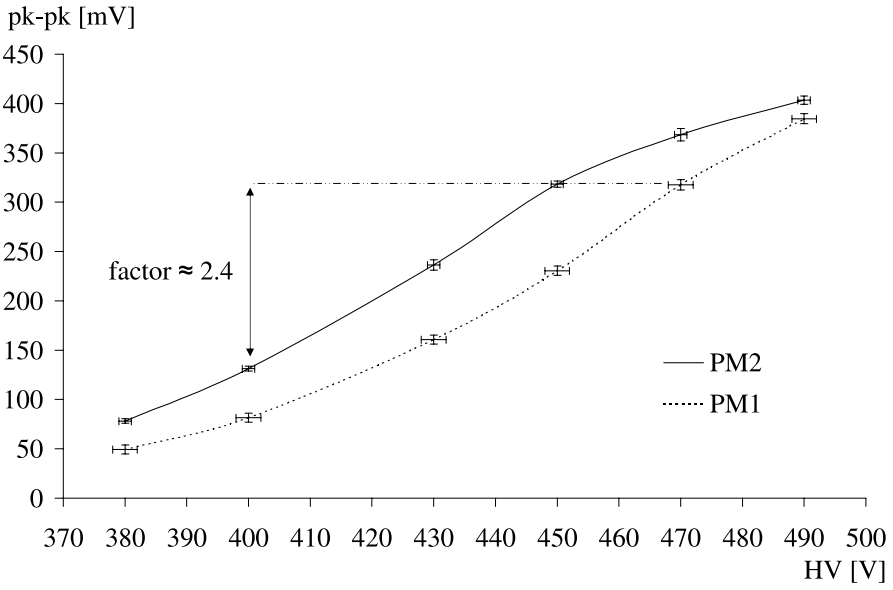

Figure 37: Results of the calibration measurements with LED.

High-Voltage or individual variations of properties of the PMs could have caused the difference between simulation and measurement.

Further measurements were done to calibrate the PMs and determine the correction factor f_{corr}. For this purpose a Light Emitting Diode (LED) was glued to an optical fiber and powered by a pulse generator (Fig. 36). Directing the light of the LED to the different PMs which were used for the measurements, allows to estimate this factor to be $f_{corr} = (2.42 \pm 0.04)$ (see Fig. 37). The measurements still differ from the simulation if this factor is considered. This might be caused by systematic errors in the simulation (see Sec. 6). Another source of systematic errors is the wavelength $\lambda_{LED} \approx 560nm$ of the LED, which differs from the emitted $\lambda_{emit} = 481nm$ of the WLS fiber. Different quantum efficiencies could change f_{corr} and therefore the differences between measurement and simulation.

The attenuation originating from the glue connection of the WLS fiber (see Sec. 5.1.1) might as well contribute to this difference as the different cable length to the CR. Where the glued connection causes an attenuation of $< 5\%$ the different cable length contributes ≈ 3 %.

Despite of these uncertainties, the estimation of the position of a beam loss is possible, if the setup is not changed. Knowing the total length of the fiber and the position of the fiber w.r.t. the beam line, allows the estimation of the beam loss position by looking up the $\ln \frac{A_1}{A_2}$ in Fig. 35. Even if the total length of the fiber and the attenuation length are unknown, the position estimation is still possible once the fiber is calibrated with at least three devices of known position.

Transforming the linear approximation extracted from Fig. 35

$$\ln\left(\frac{A_{exp,1}}{A_{exp,2}}\right) = -0.0062 \cdot cm^{-1} \cdot z + 1.6493 \tag{36}$$

to

$$z_{esti}\left(A_{exp,1}, A_{exp,2}\right) = \frac{\ln\left(\frac{A_{exp,1}}{A_{exp,2}}\right) - 1.6493}{-0.0062 \cdot cm^{-1}} \tag{37}$$

$$= \frac{\ln\left(A_{exp,1}\right) - \ln\left(A_{exp,2}\right) - 1.6493}{-0.0062 \cdot cm^{-1}} \tag{38}$$

allows to estimate the error of the longitudinal position estimation that results from the uncertainty of the logarithm of the amplitude ratio via error propagation. In addition, the error σ_{zpos} of the z position is considered (see Tab. 6). The error of the position estimation σ_{esti} is therefore

$$\sigma_{esti} = \sqrt{\left(\sigma_{zpos}\right)^2 + \left(\sigma_{exp,1} \cdot \frac{\partial}{\partial\, A_{exp,1}} z_{esti}\right)^2 + \left(\sigma_{exp,2} \cdot \frac{\partial}{\partial\, A_{exp,2}} z_{esti}\right)^2} \tag{39}$$

where the measurement with the maximum errors (Wirescanner) is considered.

$$\sigma_{esti} = \sqrt{(10.9cm)^2 + \left(-\frac{0.001}{0.011 \cdot 0.0062 \cdot cm^{-1}}\right)^2 + \left(\frac{0.0007}{0.0044 \cdot 0.0062 \cdot cm^{-1}}\right)^2} \tag{40}$$

$$\approx 31cm \tag{41}$$

which is below 50 cm (see Sec. 4.2). It has to be pointed out, that the measurement of the wire's shower is different from that of the EMSY slit masks. Obviously the dimensions of these devices are completely different. In addition, the housings of the diagnostic stations of EMSYs and Wirescanners differ at least in material thickness. This reduces the showers, but should not influence the ratio of the signal amplitudes. On the other hand, is easy to see (Fig. 35), that the measurement with the Wirescanner diverges from the almost perfectly straight line through the three EMSY measurements. But there is no clue to a systematic or accidental mistake for the Wirescanner measurement and therefore this measurement is kept in the series. The accuracy of the position estimation would rise, if a systematic error for this measurement would be considered. Additional measurement points in the series could also help to decrease the influence of the Wirescanner measurement and lower the error of position estimation. The use of fibers with shorter λ_{att} will decrease the errors too.

6 Constraints the BLM based on scintillating fibers

Continuous BLMs based on optical or scintillating fibers are limited in some points. The amount of energy deposition in the fiber depends on the amount of material that the shower travels through before. The beam line at PITZ is full of different devices. At the diagnostic stations a shower would have to pass through much more material than at the plain beam tube. Flanges may shield the fiber from secondary particles which are needed to evaluate a beam loss correctly. On the other hand, several so called *bellows* are used along the beam line. Here the material is more thin than the average beam tube. Beam losses at such positions will cause signals, that do not correspond to the known relation of signal and temperature rise. The BLM might either underestimate or overestimate the situation in cases of different material dimensions. An adapted threshold might either disturb the operation without need or risk the damage of the machine. As the damage of the machine has to be excluded, either it turns out to be possible to define safe threshold values not disturbing the usual operation or the threshold values have to depend on the position of the beam loss. The latter case would result in plenty of work, but should provide the reliable and save system demanded.

The simulations done for this work were done with very simple geometries, which are only rough approximations of the real beam line. The results are therefore first estimations and not precise predictions.
Another uncertainty in the simulations is the base material of the WLS fiber. The WLS fiber used for the measurements at PITZ has an unknown plastic base (see Tab. 4). Neither this information is available in the internet, nor in the documents at DESY in Zeuthen. The company POL.HI.TECH. could not give the information up to now. In the simulations, polystyrene was used for the WLS fiber material. Possible aging of the fibers was not considered in the simulations and calculations.

The estimation of the position of a beam loss with scintillating fibers is based on the assumption of constant attenuation along the scintillating fiber. If permanent diffuse radiation causes the pointlike attenuation at single position of a scintillating fiber, the ratio of the amplitudes will be changed and the estimation will be wrong. Radiation hard fibers are available nowadays and might lower this risk.
The temperature rise $\Delta_{inst} = 350K$ might be too high for the so called *bellows*. Bellows are intermediate elements of the beam line used to even out little vertical shifts of the beam line. Bellows are made of extremely thin (0.13 mm), folded steel (like an accordion). These might not withstand the same temperature rise as the beam tube.

7 Considerations for the integration into the BIS

A threshold value for an electronic system for beam interruption, must depend on the operation mode of the PITZ machine. In the frame of the work it was not possible to define concrete threshold values. Nevertheless it is possible to define a general structure for an decision tree. If the laser is not in operation or the laser shutter is closed, no photoelectrons are emitted and the BLM is not needed. The same is true, if the GUN power $P_{GUN} = P_{forward,GUN} - P_{reflected,GUN}$ is below some threshold. Starting from the photoelectrons being accelerated in the GUN, the BLM has to be used. Even the 5 MeV electrons after the GUN might harm the machine if 7200 bunches are dumped into the beam tube with small beam size. If in addition the BOOSTER is supplied with RF power (which is the normal operation mode), the electrons can have up to 12 MeV (current upgrade status of PITZ). In this energy regime the operation with 800 bunches of 1 nC, results in an interlock time in the order of microseconds when a beam with $\sigma = 200\mu m$ is lost (Tab. 3). The threshold values might be a combination of pulse height (peak to peak measurement for example) and number of pulses that are still allowed. The choosen values of number of pulses and the pulse height, have to depend on each other as well as on further information of the operation mode. They must scale with the charge of the bunches and must depend on whether some diagnostic devices are inserted to the beam line. The energy of the photoelectrons has to be estimated based on the effective RF power in GUN and BOOSTER and must be considered as well.
The beam size is not easily accessible but very important for the threshold value. Here, either realistic estimations for different parts of the beam line have to be used or the minimal beam size has to be choosen for the whole beam line.
There has to be a threshold applied for each bunch train and a different one monitoring the longterm heating caused by consecutive bunch trains. Effects like thermal conduction and radiative cooling, which are not considered for instantaneous temperature rise, have to be considered in the latter case. In both cases, it might be reasonable to monitor the ratio of the beam loss signals too. So, if the position of the beam loss changes, the counters for the number of pulses might be reset to 0 yielding to more stable operation.
Instead of using the BLM system based on scintillating fibers for the longterm heating, other existing detectors, for example monitoring vacuum pressure or temperature at special positions, might be useful too. A simple flow chart roughly summarizing this decision tree, is shown in Fig. 38. In addition, status information on deflecting magnets can be used to exclude beam losses behind these magnets.
The BLM should be integrated to the Beam Inhibit System (BIS) [40] already existing at PITZ. The BIS can limit operation parameters or stop the operation of PITZ if needed. It monitors parameters like RF power for GUN and BOOSTER as well as the status of diagnostic elements. These are some of the input parameters, that an BLM based on scintillating fibers would need, to adjust the threshold values to the operation modes. Beam interruption can be done in the order of milliseconds by the BIS, which is not fast enough for all possible beam losses (see Tab. 3). An electrical system, which is able to interlock the operation within few hundred nanoseconds, has to be developed. This is needed for instance, when three pulses of 0.11 μs each result in an intolerable temperature rise. If this is not possible, other action is needed. The BIS could for example increase the interlock time by limiting the bunch charge ($t_{Interlock}$: Sec. 3). When the PITZ operators have ensured the proper transport of the bunches, the charge could be increased again. Besides

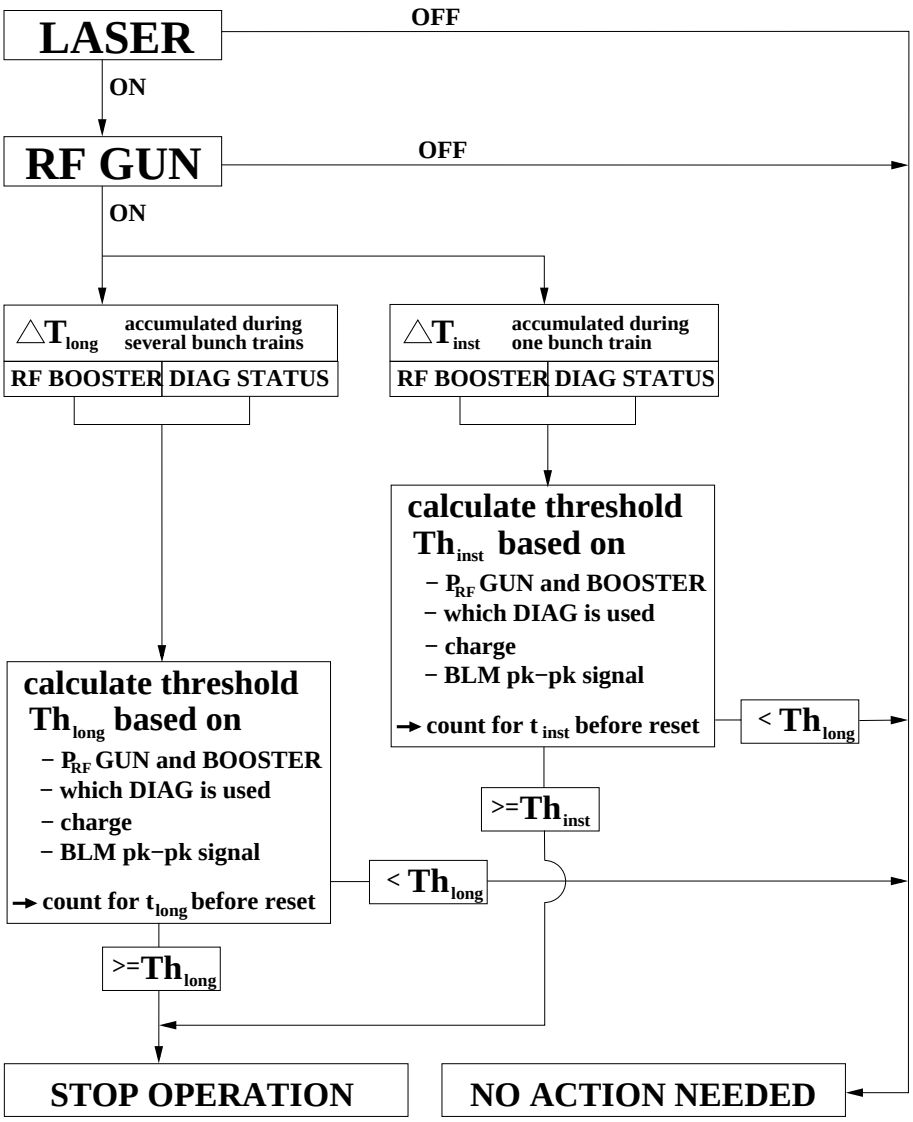

Figure 38: Roughly summarized decision tree for the BLM. Any diagnostic elements are abbreviated as DIAG. For the estimation of t_{long} cooling effects and heat conduction have to be considered.

the plain interlock function of a BLM system at PITZ, the system might as well be used for beam alignment in normal operation. A possible display structure is given in Fig. 39.

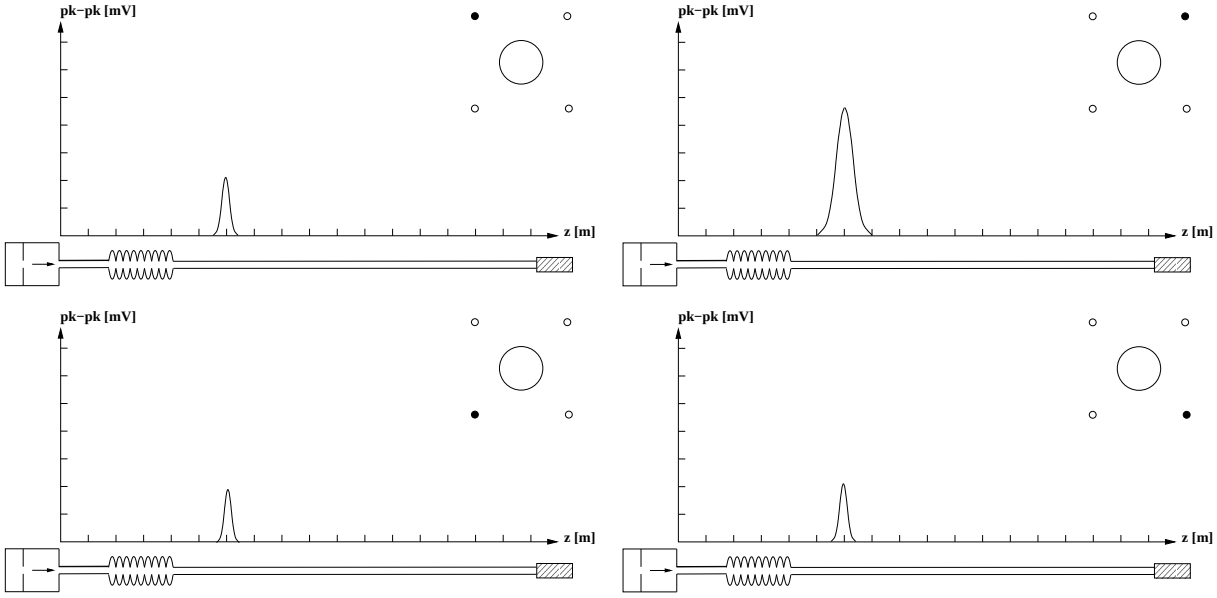

Figure 39: Possible display structure of a window for the operators of PITZ. The idea was activated by the BLPM at FLASH. Corresponding to the four fibers distributed around the beam tube, four plots could be realized. Each plot might show the z-position of any signal (regardless if harmful or not) and the signal shape (height and width). Supported with this information, the operators could determine the cause of misalignment easily in many cases. Below each z axis a sketch of PITZ (in this illustration the sketch is very rudimental) might illustrate the longitudinal position of the beam loss in addition to the plain z-value.

8 Conclusion

Calculations based on analytical formulae and Monte Carlo data were done, estimating the temperature rise in the beam tube of PITZ. Focussing on heating within 800 μs cooling effects were not considered. Considering 350 K as limit for a temperature rise within 800 μs, the required interlock time was calculated for different operation parameters of PITZ. A BLM system based on scintillating fibers was build up and tested at PITZ. It was experimentally proved that a BLM based on scintillation fibers could be used at PITZ. The obtained signals can be separated from the background without any problems. Measurements were performed and proved, that an estimation of the position of the beam loss is possible analysing the signal amplitude ratio from both ends of the scintillating fiber. The estimation of the longitudinal position of the beam loss is possible with an error of $\pm$ 40 cm. The estimation of the transverse position of beam losses was not tested at PITZ. At FLASH [33] at DESY in Hamburg this is done with four fibers around the beam tube. This should work at PITZ too, as nice signals are observed with the scintillating fibers.
The concrete threshold values needed for an integration of the BLM in the BIS of PITZ could not be specified yet.
For a BLM with scintillating fibers the next steps are:

- **Improvement of the experimental setup**
  Exchange of the used WLS fiber with a radiation hard scintillation fiber. Fibers with diameters below 1.5 mm should be considered as well. A shorter attenuation length will increase the accuracy of the position estimation. Experience with fibers longer than 4 meters in the PITZ tunnel is needed as well. A special support for the fibers, that can be permanently mounted on the PITZ support frame, has to be designed.

- **Advanced simulations**
  Simulate the beam losses including the following effects:

  - loss of heat carried by particles leaving the material [11]
  - heat conduction to the material surrounding the heated volume
  - temperature dependent energy loss

  The geometries that are used in the simulations, should include different diagnostic stations to investigate their influence on BLM signals.

- **Integration to the BIS**
  Define threshold values for all different operation modes at PITZ and assure the integration to the BIS. Advanced electronic components will be needed to assure fast interlock.

- **Precise determination of the limit for ΔT_{inst}**
  The upper limit for instantaneous temperature rise $\Delta T_{inst} = 350K$ is a rough estimation. To verify this limit, either measurements or advanced simulations have to be applied. Establishing contact to manufacturers or other experienced groups might be successful too.

The BLPM based on Cherenkov light in optical fibers as used at FLASH seems feasible at PITZ as well. A portable version of this system was developed in cooperation of DESY

and the Hahn-Meitner-Institute in Berlin [32]. The usage of such a system for interlock purpose should be possible [34].

The possibility to detect off-axis electron bunches before the complete bunch train is lost, could not be tested because of limited measurement time. A display structure like shown in Fig. 39 might be a first step in this direction.

A Mechanism of scintillation light production

Charged particles travelling through scintillating materials, cause the emission of optical photons produced in the scintillating material. Most scintillating materials are compounds of a plastic base material including aromatic rings. As plastic base normally polystyrene ($C_6H_5CH{=}CH_2$) or polyvinyltolulene (2-$CH_3C_6H_4CH{=}CH_2$) are choosen [48]. The aromatic rings are fluorescent molecules emitting photons when they are excited.
On their way through the scintillating material, charged particles excite some molecules of the plastic base material. Direct emission of ultraviolet photons by the excited plastic base molecules is dominated by energy transfer from the excited plastic molecules to the primary fluorescent molecules via resonant dipole dipole interaction (Förster [26] mechanism). This is possible, because of the high concentration ($\geq$ 1 %) of the primary fluorescent molecules which cause mean distances of $\approx$ 100 Å between fluorescent and the excited base molecules [48]. The primary fluor molecules emit UV light which is absorbed by secondary fluorescent molecules. These cause a shift to optical wavelength around 400 nm. Around 3 % of the initial energy of the excited base molecules is released as scintillation light this way [48].
A certain part of the emitted light will be absorbed by the fluorescent molecules themselves, because the absorption and emission spectra usually overlap. This causes a higher attenuation of the scintillation light in the scintillating material. Shifting the scintillation light to a longer wavelength is a possible way to reduce the attenuation.

B Physics of electromagnetic showers

High energy particles, which are sensitive for the electromagnetic force, cause electromagnetic cascades of secondary particles when travelling through matter. These cascades are also known as *electromagnetic showers* or simply *showers*. The initial particles are electrons (e^+e^-) and photons (γ). Let the cascade start with a high energetic electron. When the initial electron is deflected in the Coulomb field of electrons of the material, it emits Bremsstrahlung photons, which can decay via pair production to e^+e^- pairs. These secondary e^+e^- pairs can release Bremsstrahlung photons themselves. This leads to an exponential rise of photons and e^+e^- in the shower. As the secondary and higher order e^+e^- and γ have lower energy than their predecessor particles in each step, the cascade *dies* after a certain distance in the material. This is induced by the electron's energy falling below the *critical energy* E_{crit}. The critical energy is defined [5] as the energy, where the radiation energy losses (Bremsstrahlung) equal the collision losses (Ionisation)

$$\left.\frac{dE}{dx}\right|_{Bremsstrahlung} = \left.\frac{dE}{dx}\right|_{Ionisation} \quad . \tag{42}$$

For energies lower than the critical energy[14]

$$E_{crit} = \frac{610\ MeV}{Z + 1.24} \quad , \tag{43}$$

the energy loss of electrons in a material with atomic number Z, is dominated by ionisation processes. These do not contribute to the production of further shower particles.
The energy limit for electron pair production is obviously the duplicated electron mass $h\nu \geq 2 \cdot m_e \approx 1.022 MeV/c^2$.
The longitudinal extension of the energy deposition caused by the shower depends on the material and the initial particle's energy E_{in}. The profile can be described by a gamma distribution [36] with the maximum energy deposition [49] at

$$\frac{x}{X_0} = \ln\left(\frac{E_{in}}{E_{crit}}\right) + \begin{cases} -0.5 & : \text{ incident electron} \\ +0.5 & : \text{ incident photon} \end{cases} \tag{44}$$

where X_0 is the radiation length and x the travelling length in the material. The transverse dimensions of the shower are best described with the Molière radius R_M which is defined [49] as

$$\frac{1}{R_M} = \frac{1}{\sqrt{4\pi/\alpha} \cdot m_e c^2} \sum_j \frac{w_j \cdot E_{crit,j}}{X_{0,j}} \tag{45}$$

for compound materials. Here, α is the *fine structure constant*, c the speed of light, w_j the weight fraction of a compound of the material and $E_{crit,j}$ and $X_{0,j}$ its critical energy and radiation length. If the material is no compound this simplifies to $R_M = \frac{X_0 \cdot \sqrt{4\pi/\alpha} \cdot m_e c^2}{E_{crit}}$.

[14] an approximation for solids and liquids [16]

C Simulation tools

The local temperature rise in the beam tube in case of beam loss is a central point of this work. Measurements would be difficult due to the problem of precise temperature measurement at a very small hot volume inside the beam tube. The prediction of the position of this volume itself would be difficult enough, but temperature measurements are not possible at the inner surface of the tube when this position is hit by the beam. Hence, simulations have to be applied to predict the temperature rise of the beam tube in case of energy deposition caused by a beam loss.
The energy deposition in the sensitive parts of the BLM corresponding to intolerable beam losses have to be predicted by simulations, too. For this purpose, showers were produced by insertion of diagnostic devices. The same devices were integrated in the simulations to relate the simulations to the measurements.
To increase the trust in the simulations, two different simulation tools were applied and are described in the following.

C.1 GEANT3.21

GEANT3.21 [28] (called GEANT in the following) is a FORTRAN77 [46] based detector description and simulation tool for high energy physics. It is part of the CERN library [12] and is licensed under the *GNU General Public License* [29]. GEANT simulates the passage of particles through matter, i.e. the transport of the particles and their interaction with matter on their path is calculated based on the chosen physical effects and the known properties of particles and matter. The particles simulated can be generated with external Monte Carlo generators.
In GEANT, the setup is composed of user implemented volumes, which are positioned in a superior mother volume, including all other volumes. Each volume is assigned to a *tracking medium*. It is possible to assign several volumes, which do not need to be connected, to the same tracking medium. Each tracking medium itself is assigned to a homogen material and connected to several values for different transport properties.
A graphical representation of the user implemented setup and the particles' path through it is possible with the interactive version of GEANT. Such figures is shown in Fig. 40 and 41. This allows effective debugging in many cases. The transport (called *tracking* in GEANT) is done in single steps with material specific step length. The calculated energy loss of each step can be accessed via the variable *DESTEP*.
The standard units of GEANT are second (time), centimeter (distance), kilogauss (magnetic field force), GeV (energy), $GeV \cdot c^{-1}$ (momentum) and $GeV \cdot c^{-2}$ (mass).

C.2 FLUKA2005 (version 6.0)

FLUKA2005 (version 6.0) [22,23] (called FLUKA in the following) is a multi-particle transport code like GEANT and was developed for simulation of particle transport and interaction with matter. Electrons and photons in the range of 1 keV up to several PeV can be virtually transported by FLUKA.
FLUKA uses a Combinatorial Geometry based on the geometry package of MORSE [20]. Here, bodies are defined and joined to regions by logical subtraction, intersection or union. All regions are placed in the so called *black hole* region which corresponds to the

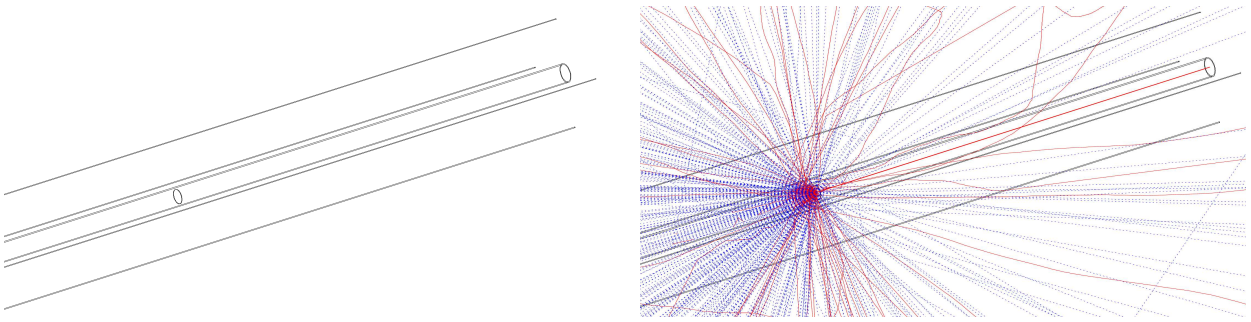

Figure 40: GEANT plot of a typical PITZ geometry as used for this work. The left side without electrons and with 200 electrons of 12 MeV on the right side. The cylindric plate inside the beam tube is of 1 mm tungsten.

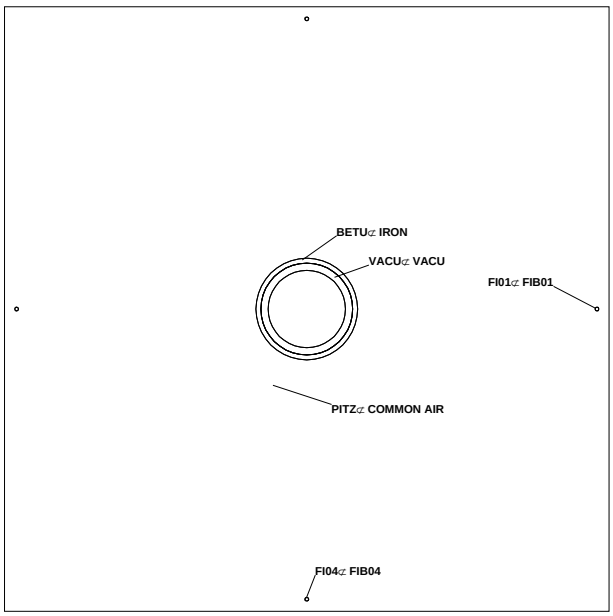

Figure 41: A cross section view of the geometry of Fig. 40. The labeling of volumes can be done interactively with GEANT. Labeling of the cylindric plate, shown as the most inner circle, was not possible, because the vacuum is surrounding the plate.

superior mother in GEANT. Regions do not have to consist of connected bodies. Each region is assigned to a homogen material.
The scoring of energy deposition is very similar to GEANT. In FLUKA the scored properties are normalized to one particle and listed per region. In the plots of setup including data, densities are shown instead of absolut values (see Sec. 5.4 or 5.3 for plot examples). To obtain absolute values, the user has to multiply the density values with the wanted number of particles. The standard units in FLUKA are equal to these of GEANT.

D Acknowledgments

The work on my diploma thesis was supported by several people. My sincere thanks go to them.
Prof. Dr. Nikolaj Pavel teached me, that it is right to ask if things are not clear. My deepest sympathy and condolence to his relatives and friends can not express the loss his death means to us.
Hermann Kolanoski started supervising me in February 2006 and gave helpful suggestions. Hans-Jürgen Grabosch and Sabine Riemann greatly supervised me during my work at PITZ. Thank you very much!
Thanks to DESY at Zeuthen, where I could work on this thesis. The members of the PITZ group at Zeuthen welcomed me and helped me whenever I asked for help. John Maidment and Gunnar Priebe greatly supported my measurements at the proton accelerator DESY3 in Hamburg. Peter Pohl from DESY at Zeuthen greatly prepared all fibers for my measurements.
Last, but not least at all, I thank my parents for their general and financial support during my studies at University. My own family, consisting of Janine, Florian and Luca Bräuer are the most important part of my life. Thank you for being!

References

[1] AIRCOM, *aircom plus* manufactured by SSB Elektronik GmbH, Iserlohn/Germany, www.ssb.de
http://www.ssb.de/pdf/DB-AircomPlus-D.pdf

[2] David E. Alburger: *The Decay of Rh^{106}*, Physical Review, Volume 88 Number 2, October 1952

[3] O.C. Allkofer, P.K.F. Grieder, "Cosmic rays on Earth", Physics Data 25-1, Fachinformationszentrum Energie Physik Mathematik GmbH, Karlsruhe (1984)

[4] E. C. Aschenauer and J. Baehr and V. Gapienko and B. Hoffmann and H. Luedecke and A. Menchikov and C. Mertens and R. Nahnhauer and R. Shanidze, "Testrun results from prototype fiber detectors for high rate particle tracking", NUCL.INSTRUM.METH.A, Vol. 424, p.459, 1999

[5] M.J. Berger, S.M. Seltzer, "Tables of Energy Losses and Ranges of Electrons and Positrons", National Aeronautics and Space Administration Report NASA-SP-3012, Washington DC, 1964

[6] BERGOZ Instrumentation, www.bergoz.com

[7] BERGOZ, [Manual of the BLM], http://www.bergoz.com/products/BLM/BLM-downloads/files/BLM.Manual%201.6.PDF

[8] BERGOZ, [Technical note],
http://www.bergoz.com/products/ICT/Downloads/files/ICT.Tech.note.06-1.pdf

[9] Bicron Brochure, Bicron, Newbury, Ohio, October 1993

[10] R.K. Bock, A. Vasilescu, "The Particle Detector BriefBook", Springer-Verlag, Berlin, 1998

[11] J. Bosser et al., "The micron wire scanner at the SPS", Technical Note (SPS-86-26-MS), CERN, 1986, http://doc.cern.ch//archive/electronic/other/generic/public/cer-000085648.pdf , p.11-14

[12] CERNLIB, http://cernlib.web.cern.ch/cernlib/

[13] DESY, Deutsches Elektronen Synchrotron, www.desy.de

[14] Dortmunder Electronen Testspeicherring Anlage, University of Dortmund, Dortmund, Germany, http://www.delta.uni-dortmund.de/

[15] S. Eidelman et al. [aka Particle Data Group], Particle Physics Booklet (p.233), Extracted from the *Review of Particle Physics*, Physics Letters B, Volume 592, 1 (2004)

[16] ibid., p.248

[17] ibid., p.317

[18] ELBE at FZ Rossendorf, Germany, www.fz-rossendorf.de/ELBE

[19] type TR21301-FRNC-b, el-spec GmbH, www.elspec.de, contact: info@elspec.de

[20] M.B. Emmett, *The MORSE Monte Carlo radiation transport system*, Oak Ridge National Laboratory report ORNL-4972 (1975), Revision: ORNL-4972/R1 (1983), Revision: ORNL-4972/R2 (1984)

[21] ESTAR, *Stopping Powers and Ranges for Electrons*, http://physics.nist.gov/PhysRefData/Star/Text/ESTAR.html

[22] A. Fassò, A. Ferrari, J. Ranft, and P.R. Sala, "FLUKA: a multi-particle transport code", CERN?2005?00X, INFN TC 05/11, SLAC?R?773, 31 August 2005

[23] A. Fassò, A. Ferrari, S. Roesler, P.R. Sala, G. Battistoni, F. Cerutti, E. Gadioli, M.V. Garzelli, F. Ballarini, A. Ottolenghi, A. Empl and J. Ranft, The physics models of FLUKA: status and recent developments Computing in High Energy and Nuclear Physics 2003 Conference (CHEP2003), La Jolla, CA, USA, March 24?28, 2003, (paper MOMT005), eConf C0303241 (2003), arXiv:hep-ph/0306267

[24] FLASH, Free electron LASer in Hamburg - FLASH at DESY-Germany - www.desy.de

[25] K. Flöttmann, F. Stephan, "Proposal for the BMBF *RF Photoinjectors as Sources for Electron Bunches of Extremely Short Length and Small Emittance*", 1999, http://adweb.desy.de/pitz/web/tuovi/bmfb_01_englisch_og.pdf

[26] Th. Förster, "Zwischenmolekulare Energiewanderung und Floureszenz", Ann. d. Phys. 2 (1948), p.55

[27] D. Frekers, A scintillating fiber detector for neutrino physics at the TRIUMF-Kaon factory, Workshop on Application of Scintillating Fibers in Particle Physics, Blossin, September 1990

[28] GEANT - Detector Description and Simulation Tool CERN Program, Library Long Writeup W5013, CERN Geneva, Switzerland

[29] GNU, http://www.gnu.org/licenses/licenses.html#GPL

[30] Hamamatsu, [Manual of the PM]
http://sales.hamamatsu.com/assets/pdf/parts_R/TPMH1294E01.pdf

[31] H. Henschel, J. Kuhnhenn, M. Körfer and F. Wulf,"Optical fibre dosimeter for SASE FEL undulators", *Prepared for 6th European Workshop on Beam Diagnostic and Instrumentation for Particle Accelerators (DIPAC 2003), Mainz, Germany, 5-7 May 2003*

[32] HMI, Hahn-Meitner-Institut, Standort Berlin-Wannsee, www.hmi.de

[33] M. Körfer, W. Göttmann, F. Wulf and J. Kuhnhenn, "Beam loss position monitor using Cerenkov radiation in optical fibers", *Prepared for 7th European Workshop on Beam Diagnostics and Instrumentation for Particle Accelerators (DIPAC 2005), Lyon, France, 6-8 Jun 2005*

[34] M. Körfer, FLASH, markus.koerfer@desy.de, private communication

[35] W. Kunz, J. Schintlmeister: *Tabellen der Atomkerne*, Akademie-Verlag Berlin, 1958

[36] E. Longo, I. Sestili, "Monte Carlo Calculation Of Photon Initiated Electromagnetic Showers In Lead Glass", Nucl. Instrum. Meth. Volume 128, 1975, p.283 [Erratum-ibid. **135** (1976) 587].

[37] A. Oppelt, www-zeuthen.desy.de/∼apohl/pitz2

[38] PAW - Physics Analysis Workstation, CERN Program Library Long Writeup Q121, CERN Geneva, Switzerland

[39] PITZ, http://adweb.desy.de/pitz/web/

[40] M. Pohl,"Protocol for the Profibus Communication between the Beam Inhibit System (BIS) and the PITZ Control System (CS)", PITZ internal note, Sept. 2006

[41] POL.HI.TECH., www.polhitech.it, type: POLIFI S248-150

[42] Remanit 4306 steel, [data sheet on material properties], www.edelstahl-witten-krefeld.de/upload/binarydata_ewkinterd4cms/1383/ REMANIT_4306_de.pdf

[43] type RG 174, DESY Lager Nr. 11 109, normally used in connection with ®LEMO connectors

[44] Prof.Dr.H. Stöcker, *Taschenbuch der Physik*, 4., korrigierte Auflage, Verlag Harri Deutsch, 2000, ISBN 3-8171-1628-4, p.704 and p.693

[45] K. Wittenburg,"Beam loss detection," *Prepared for 1st European Workshop on Beam Instrumentation and Diagnostics for Particle Accelerators, Montreux, Switzerland, 3-5 May 1993*

[46] Wikibook on FORTRAN77, http://de.wikibooks.org/wiki/Fortran:_FORTRAN_77

[47] WOLFRAM, http://mathworld.wolfram.com/IntegerPart.html

[48] W.-M. Yao et al. aka Particle Data Group, Review of Particle Physics, Physics Letters B, Volume 592 (2004), p.254

[49] ibid., p.250

[50] ibid., p.255

Erklärung

Die vorliegende Arbeit habe ich ohne unerlaubte fremde Hilfe angefertigt und nur die angegebene Literatur und Hilfsmittel verwendet.
Meine Diplomarbeit darf in der Bibliothek der Humboldt-Universität zu Berlin ausgelegt werden.

Peter Spanknebel
Berlin, 30. September 2006